Coupled Flight Mechanics based on Reduced Order Models for use in Tiltrotor Stability Analysis

4 authors, including:

James Wakefield
University of Bristol
1 PUBLICATION   **2** CITATIONS

Dorian Jones
University of Bristol
80 PUBLICATIONS   **690** CITATIONS

Coupled Flight Mechanics based on Reduced Order Models for use in Tiltrotor Stability Analysis

J. E.G. Wakefield *, S. M. Cassillas* , A. L. Gaitonde† , and D. P. Jones †
Department of Aerospace Engineering, University of Bristol, United Kingdom, BS8 1TR

The development of two coupled stability models is presented. The models are based on the reduced order modelling of an Unsteady Vortex Lattice Method (UVLM) computational fluid dynamics code that provides an explicit wake model, coupled with classical rigid body equations of motion. These have been derived to include all 12 states to accommodate a full dynamic wake response. The model retains the entirety of the linear dynamics of the reduced order aerodynamics in the stability analysis, neglecting the need for aerodynamic derivatives. This allows for rapid and accurate force response and flow solution reconstruction. A new Linear Time Periodic balanced model reduction is developed, as well as an ensemble-averaging approach which may allow for a much lower computational cost than the full periodic stability. Further investigation is required to prove the equivalence of the two approaches. Validation studies have been performed to show the accuracy offered by the coupled model. An investigation into the stability of the XV-15 in comparison to an equivalent classical model was performed, showing similar eigenvalue distributions but with the ensemble-average coupled model producing larger magnitude instabilities. An investigation into the reconstruction of flow solutions during unstable motions was performed, allowing significant insight into the aerodynamics and showing potential for use as a design tool.

I. Introduction

The aim of this work is to investigate the use of reduced order coupled models in stability analysis and their added capability as a preliminary design tool via solution reconstruction. A large body of research exists in terms of determining the stability of both aircraft and rotorcraft by accurately calculating the dynamic stability derivatives through various CFD simulation techniques. Using CFD in a non-inertial frame allows the dynamic derivatives to be expressed as moving grid and 'grid velocity' components [1, 2]. Sensitivity analysis can be used to reduce the computational expense directly [1, 3]. However, most of this research has focused on obtaining accurate stability derivatives through high accuracy flow simulations, and there are only a few mentions of the time history of the flow in the context of rotary motions. The assumption of quasi-steady flow is usually applied and this allows a Taylor series linearisation of the solution around an instant in time. However, although this assumption has been shown to be accurate for aircraft, it would seem unreasonable to ignore the time-history effects due to the wake shed by the rotor in a tiltrotor aircraft. The wake has a strong interaction with the blades and the wing, altering the system dynamics at the blade passing frequency. Research exists involving frequency domain analysis of periodic aerodynamic effects [4], and the so called 'unsteady sensitivity equations' [5]. However, the stability derivatives are still calculated through a Taylor expansion and a linearisation in time.

This desire to include the time history effects with a reasonable computational expense is the rationale behind this work. Reduced order state space models of the aerodynamics are developed and then coupled to the rigid body mechanics. To investigate the effect of using the quasi-steady Taylor-series, the results are compared to the same aerodynamic models if basic classical analysis had been used. The coupled stability is considered for two representations of the aerodynamics. A Linear Time Periodic (LTP) model of the perturbation aerodynamics seems the most appropriate for tiltrotor applications. Here, a new method of periodic balanced model reduction is developed which has further possible implications for both periodic system identification and realisation. Secondly, an ensemble (or period) averaged aerodynamic model is analysed, which may be accurate for "slow" instabilities such as the fountain flow found in tiltrotors. The XV-15 tiltrotor in hover is investigated as a demonstration of the methods developed

---

*Master's Student, Department of Aerospace Engineering, jw15268@my.bristol.ac.uk

†Reader in Aerodynamics, Department of Aerospace Engineering, Dorian.Jones@bristol.ac.uk

A. Tiltrotor Aircraft: Unique Aerodynamics Dynamics and Stability

Rotorcraft are an undoubtedly versatile variant of aircraft, their Vertical Take-Off & Landing (VTOL) and hover capability have led them to be employed in a variety of both civil and military applications. However, this vertical lift capability comes at a cost. Rotorcraft tend to be less efficient in cruise, with shorter range and lower cruise speed relative to fixed-wing aircraft. The motivation for rotorcraft designers is thus to improve upon these drawbacks, an effort which has led to a variety of concepts that aim to supersede the conventional penny-farthing rotor configuration. Arguably, the most viable of these concepts are the compound helicopter and the tiltrotor configurations. Enabled by advancements in computer-aided design methods and composites materials, these configurations have seen a resurgence in their popularity in recent years, made apparent by programmes such as the Fast Rotorcraft Innovative Aircraft Demonstrator Platform of Clean Sky 2 [6] and the United States Armed Forces Future Vertical Lift programme [7]. The military potential of tiltrotors has been realised by the Bell Boeing V-22 Osprey, and for civil markets the Leonardo AW609 will be the first civil tiltrotor to enter into service [8].

Tiltrotors resemble a conventional fixed-wing aircraft, but with large diameter proprotors mounted on nacelles located at the wing tips. These nacelles can tilt the axis of rotation to be perpendicular to the wing chord line for axial flight/hover (helicopter mode) or parallel to the chord line for forward flight (fixed-wing mode). The transition state between these two modes also gives the option for a Short Take-Off and Landing (STOL) capability, which is typically more efficient than VTOL. This ability to tilt the proprotors allows the axis of rotation to remain aligned with the onset flow in all flight conditions, thus eliminating the speed-limiting effects of retreating blade stall and advancing blade compressibility present in typical helicopters. Hence, tiltrotors tend to provide superior performance relative to compound helicopters in the cruise condition [9], typically having a speed and range comparable to a propeller-driven fixed-wing aircraft.

Due to their complexity, the stability analysis of tiltrotor aircraft relies heavily upon the classical methods developed for conventional fixed-wing or conventional helicopter configurations. However, whilst these methods are well established for such aircraft, the stability of tiltrotors is less well understood due to both the complexity of tiltrotor aerodynamic/structural characteristics and the relatively short history of tiltrotor development. This deficiency in the modelling of tiltrotors has been made apparent on numerous occasions for both the V-22 (see for example [10]) and during flight testing of the AW609. In the case of the AW609 the accident occurred during high-speed dive testing, in which the flight control system failed to allow the pilots to adequately compensate for an unexpected dutch-roll-type instability. This motion led to excessive proprotor

Fig. 1 **The fountain flow effect between the proprotors and the wing for a tiltrotor aircraft in hover.**

flapping due to the large yaw oscillations (and hence excessive sideslip values), in turn causing multiple contacts between the proprotors and the wings and the in-flight breakup of the aircraft [11]. The dynamics of this instability and the effect it had on the large diameter proprotors could not be predicted (or indeed replicated) by the project simulator [11], which highlights the necessity for the development of more comprehensive analysis methods.

The majority of the unconventional instabilities that are known to occur in tiltrotors stem from the interaction between complex proprotor-related aerodynamics and the unique structural configuration of the aircraft. A prime example of this is the fountain flow effect, which is visualised in Figure 1. This is a phenomenon unique to tiltrotors in axial flight, in which part of the wakes from each proprotor deflect inboard along the wing span and then is redirected upwards where they meet along the fuselage centre-plane. This slow-moving wake is then re-ingested by the inboard portion of the proprotor discs, creating a region of recirculating air and causing a reduction in inflow velocity, and thus thrust, over that portion of the rotor disc [12, 13]. Movement of the axis of this fountain flow, for instance via a gust, can lead to stability issues from the varying thrust between the proprotors.

Figure 2 also highlights a secondary fountain-flow-type effect that occurs when the tiltrotor hovers In Ground Effect (IGE). This flow is formed by a similar mechanism except that it reflects off the ground instead of the wing, seen in the upper portion of Figure 2, and the resulting fountain deflects upwards onto the underside of the airframe, as seen in the lower portion of Figure 2. Due to the forward/aft asymmetry of tiltrotors, where the aft section of the aircraft presents a larger area due to the tailplane than the forward section, this impingement tends to generate a nose-down pitching moment, leading to a mode of instability IGE [14]. Roll instability can also occur if the centre-plane of the fountain in the upper portion of Figure 2 moves laterally, impinging asymmetrically upon the underside of the wings for
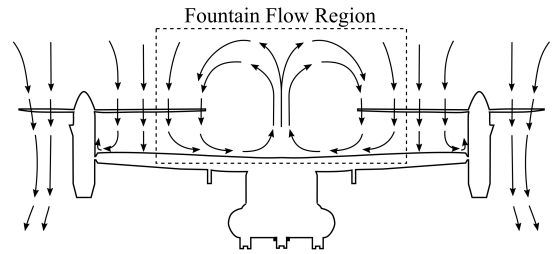
instance due to gusts or non-zero sideslip angles. The Generic Tiltrotor Simulator (GTRS) developed by NASA [14] failed to account for such instabilities via a quasi-static aerodynamic model, especially in the case of the roll instability, the prediction of which was still inaccurate after utilising empirical corrections. This modelling failure arose due to insufficient modelling of the proprotor wakes and their interaction with the airframe [14], and Kleinhesselink in the development of her classical tiltrotor stability model [15] also notes the benefits a full wake model would bring to the fidelity of her stability analysis.

The aerodynamics involved in tiltrotor stability is clearly dynamic, and the proprotor wakes appear to interact strongly with the rest of the airframe to a higher degree than would be seen in a conventional fixed-wing or rotorcraft configuration. This, along with the turbulent history of tiltrotor development, begins to cast doubt over the classical flight mechanics methods, which treat aerodynamic forces as a series of aerodynamic derivatives (i.e. first or second order Taylor series approximations) in the equations of motion. With this motivation in mind, this paper investigates alternative methods of analysing the stability of unconventional aircraft configurations such as tiltrotors. This is done via the use of a coupled flight mechanics model, which treats the flight mechanics equations of motion and aerodynamics as two, coupled linear systems, thus retaining the linear dynamics of the aerodynamic system in the analysis.

B. Outline of Paper

The development of such a coupled flight mechanics model is presented for a generic tiltrotor based upon the Bell XV-15 [16]. This model couples a Reduced Order Model (ROM) of an Unsteady Vortex Lattice Method (UVLM) aerodynamics model with a generalised, rigid body flight mechanics model. The UVLM aerodynamics provide a cost-effective explicit wake model suitable as a prototype Computational Fluid Dynamics (CFD) code to investigate the use of the ROM in the coupled model. Future work can replace this with a higher fidelity CFD

Fig. 2   The secondary fountain flow effect between the proprotors and the ground for a tiltrotor aircraft in hover.

code, such as a Reynolds-Averaged Navier-Stokes solver, without impact on the methodologies presented. The flight mechanics model used is similar to the classical flight mechanics equations of motion except it retains the Centre of Gravity (CG) linear displacement perturbation states (x, y, z) and the heading (yaw) angle perturbation state (ψ) to fully capture the dynamics of the explicit wake model. Again, the modularity of the model allows for simple replacement with a higher fidelity treatment of proprotor dynamics or drive system modelling if desired for future work. The periodicity of the system is treated in two ways. Firstly, a new efficient and robust methodology for constructing numerically balanced ROMs for linear time periodic systems is presented. This represents a direct extension of the Eigensystem Realisation Algorithm (ERA) methodology to linear time periodic systems and its equivalence to a balanced Proper Orthogonal Decomposition (POD) is highlighted. The second approach investigated is based on an ensemble-average of the periodic response and forms an equivalent linear time invariant (LTI) model. This approach shows much promise for significantly reducing computational expense compared to the full periodic analysis, and as such aligns well with the motivation for bringing the stability analysis into preliminary design for systems such as tiltrotors.

The use of the ERA to produce a ROM provides a vast reduction in computational cost for modelling the aerodynamic system. In addition to modelling the Input-Output (IO) behaviour of the system, simply via observation of the impulse response outputs of the UVLM code (notably without requiring modification to the code itself), the ERA also allows the calculation of the normal POD modes. This ability allows for the reconstruction of flow solutions such as pressure coefficients from the states of the coupled model. This offers the ability to investigate flow behaviour (for instance the behaviour of the fountain flow) during unstable motions for very little computational expense. For future tiltrotor design this investigative power has potential in the design of passive and/or active measures for stabilising modes of motion. For example; if it is found that a particular flow phenomena, such as a shifting fountain flow, destructively interacts with the flight mechanics system to cause the unstable mode, then the reconstruction of this flow could allow designers to
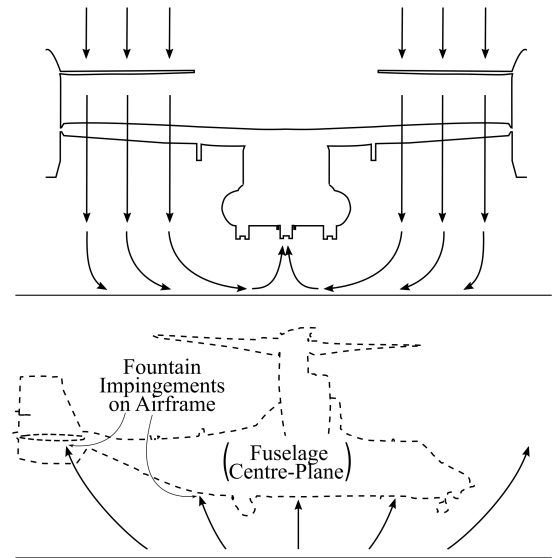
modify the aircraft topology to passively stabilise the system.

II. Flight Mechanics Model
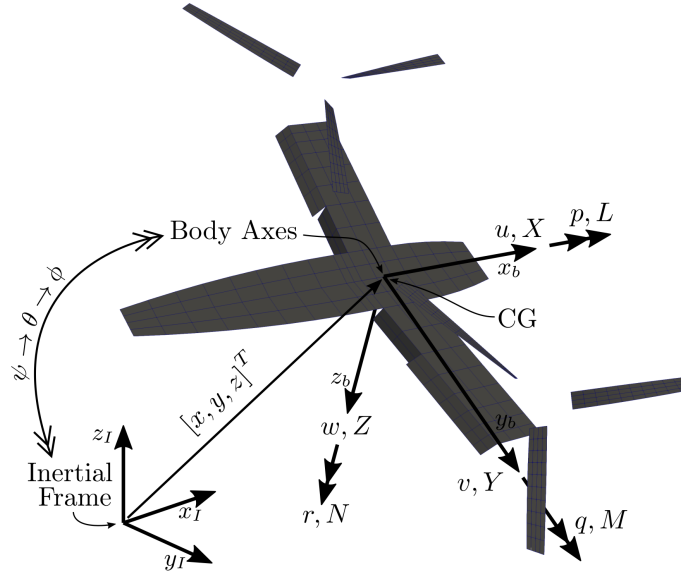
A. Overview of Flight Mechanics

Fig. 3   Flight mechanics axes convention.

Classical three-dimensional rigid-body flight mechanics equations of motion are used in this work to describe the motion of the aircraft due to the application of external, aerodynamic forces. Despite the rigid-body assumption limiting the applications of such a model, it is well known that these equations tend to represent the motion of aircraft to a reasonable degree, especially for preliminary design purposes [17, 18]. Efforts have been made in this work to enhance the fidelity of the flight mechanics model by incorporating gyroscopic contributions into the angular momentum (and thus the moment) equations of the system as per Etkin and Reid [18]. However, a notable deficiency of the model arises from a lack of blade flapping freedom. The XV-15 proprotors are stiff in-plane, which implies little motion in the lead-lag degree of freedom (DoF). However, each proprotor has gimbal-mounted blades [16], which permits cyclic and collective blade pitch changes (and indeed other sources of aerodynamic loading) to translate into longitudinal and lateral 'rigid' flapping motion of the entire 3-blade proprotor system, much like a 2-bladed 'teeter' helicopter rotor does. The development of a high-fidelity tiltrotor model, however, is not the focus of this paper and so such extensions are recommended for future work.

The general form of the non-linear equations of motion is given by:

$$\underline{\dot{x}}_{FM} = \underline{f}(\underline{x}_{FM}, \underline{y}_A, \underline{W}, t) \tag{1}$$

where it is noted that the aerodynamic force vector can be a function of any number of control inputs $\underline{u}$. For the full overview of the non-linear equations and their derivation the reader is referred to Chapter 4 of Etkin and Reid [18]. The two vectors $\underline{x}_{FM}$ and $\underline{y}_A$ are defined in Equations (2a) and (2b) as the state vector of the flight mechanics system and the aerodynamic load vector acting on the flight mechanics system respectively, and $\underline{W} = \left[W_x, W_y, W_z\right]^T$ is the wind velocity vector relative to the inertial frame, expressed in the body axes coordinate system.

$$\underline{x}_{FM} = [x, y, z, u, v, w, \phi, \theta, \psi, p, q, r]^T \tag{2a}$$

$$\underline{y}_A = [X, Y, Z, L, M, N]^T \tag{2b}$$

The notation is as follows, and visualised in Figure 3 for clarity. The vector $[x, y, z]^T$ is the position of the CG relative to the origin of the inertial (Earth-fixed) frame in the coordinate system of the inertial frame. The vector

$[u,v,w]^T$ is the velocity of the aircraft CG relative to the wind vector $\underline{W}$, expressed in the body axes coordinate system. The vector $[\phi,\theta,\psi]^T$ defines the Euler angles of the aircraft's orientation relative to the inertial frame in the typical order of yaw-pitch-roll from inertial to body axes frame. The vector $[p,q,r]^T$ defines the aircraft rotational velocities about the body axes. The vector $[X,Y,Z]^T$ denotes the net external force acting upon the aircraft acting at CG and expressed in the body axes coordinate system, and $[L,M,N]^T$ denotes the net external moment acting at the aircraft CG, again about the body axes.

As per most classical flight mechanics analyses, the non-linear system can be linearised about an equilibrium $\bar{\underline{x}}_{FM}$, referred to as a trim solution. Each of the variables within the vectors $\underline{x}_{FM}, \underline{y}_A, \underline{W}$ are expanded as the sum of the non-linear equilibrium $\bar{\cdot}$, and small perturbation $\Delta\cdot$. Applying the small perturbation assumption throughout the system of equations and changing notation by dropping the Δ allows the formation of a linear system of equations describing the linear dynamics of the aircraft about the trim condition.

At this point the formulation of the flight mechanics system for the coupled model diverges slightly from classical methods, as no extra assumptions regarding the system are made. A notable result of this is that the states (x,y,z) are retained, whereas classical methods typically remove these (often along with the heading angle ψ) with the assumption that these states have no effect on the aircraft dynamics. However, here it is noted that the wake modelling provided by the UVLM does provide a force response at the body axes due to perturbations in any of these four flight mechanics states, and for this reason they are not neglected. The full, linearised flight mechanics equations can be found in Appendix A for completeness. With the assumption that the aircraft is operating in still air with no gusts such that $\bar{W} = \underline{W} = \underline{0}$. The flight mechanics system representing local behaviour about the trim solution can be written in matrix form as:

$$\underline{\dot{x}}_{FM} = A_{FM}\underline{x}_{FM} + E_{FM}\underline{y}_A \tag{3}$$

where A_{FM} represents the kinematics, E_{FM} the inertias of the system, and $\underline{x}_{FM}$ is the perturbation in the 12 state, state vector. It is assumed that the aircraft is a rigid body with rigid spinning rotors attached, the non-rotating hub axes of the rotors are fixed relative to the body axes, and the x_b-z_b plane is one of symmetry so the inertias $I_{yz} = I_{xy} = 0$. It will be seen in Section II.C that retaining the external forces $\underline{y}_A$ as the effective input vector avoids the need for extracting aerodynamic and/or control derivatives, and allows for direct coupling to the aerodynamic ROM system. Effectively this allows for arbitrary control inputs, all of which are dealt with within the UVLM-ROM system. The analysis performed here is, however, stick-fixed such that the control inputs become $\underline{u} = \underline{0}$.

B. Unsteady Vortex Lattice Method Aerodynamics

This work uses the incompressible, inviscid UVLM code developed by Roth [19] as a prototype CFD code for these investigations. UVLM aerodynamics provides a low-fidelity CFD method well-suited to the more detailed preliminary design/analysis of control systems, stability, coupled flight mechanics and aeroelasticity problems [19, 20]. Critically, for this work, it also provides the explicit modelling of aerodynamic wakes via the shedding of vortex panels/particles without the need for a volume mesh. The use of free vortex particles to represent wakes (as opposed to panels) in the UVLM code avoids problems with wake sheet roll-up, and have been found to provide the most accurate vorticity distribution and evolution of the wake sheet [19]. As noted by Kleinhesselink [15], a lack of an explicit wake model is a deficiency of many tiltrotor stability models. It is well known that the proprotor wake behaviour in tiltrotor aircraft is complex, and when in helicopter mode the wake strongly interacts with both the wing, via strong downloads (see [21–23]), and the proprotors, via the fountain flow effect (see [12]) discussed in Section I. The inclusion of a wake model not only improves model validity, but also enables one to analyse the behaviour of the wake during the evolution of unstable coupled modes via the solution reconstruction methods outlined in Section III.C. For more detail on the theory behind UVLM the reader is referred to Katz and Plotkin [24].

The tip Mach number for an XV-15 hovering in still air is approximately $M = 0.691$ given standard sea level conditions, thus the UVLM will start to lose accuracy due to compressibility effects for this analysis. However, as previously stated the aim of this work is not to provide a high-fidelity tiltrotor model of the XV-15, but instead to investigate the use of a coupled model in stability analysis and its added capability as a design tool via solution reconstruction.

C. Coupled Model Formulation

For the case of the stick-fixed analysis where we have no control inputs (noting that $\underline{x}_{FM}$ is effectively the aerodynamics input vector), the general aerodynamics system can be written as per Equation (4). Here f and g are

non-linear functions and $\underline{x}_A$ is the state vector of the aerodynamic system.

$$\dot{\underline{x}}_A = \underline{f}(\underline{x}_A, \underline{x}_{FM}, t)$$
$$\underline{y}_A = \underline{g}(\underline{x}_A, t)$$

(4)

Similar to Section II.A, the assumption is made that for a small region about some equilibrium, where $\underline{x}_A$ is the trim condition, the system is approximately linear. Therefore the dynamics of this system in the small region around this non-linear trim condition can be represented by a linear system of equations. Noting that the UVLM provides a discrete representation of the aerodynamics, while $\underline{x}_k$ & $\underline{y}_k$ now refer to perturbations about the trim state at timestep k, the aerodynamic system can be written as:

$$\underline{x}_{k+1} = A_k \underline{x}_k + B_k \underline{x}_{FM,k}$$
$$\underline{y}_k = C_k \underline{x}_k$$

(5)

The (A_k, B_k, C_k) triple of this system needs to be identified, however it is prohibitively large and so would lead to massive computational expense. Thus, a ROM is used to form an r dimensional system. In this work, the reduced form of the UVLM perturbation response about the trim condition is written as either a LTI or LTP system. As we are dealing with linear stability then using a linear system is appropriate, and although the system is periodic we will investigate the use of an invariant system as an approximation. The reduced system can therefore be written as either

$$\underline{x}_{r,k+1} = A_{r,k} \underline{x}_{r,k} + B_{r,k} \underline{x}_{FM,k}$$
$$\underline{y}_k = C_{r,k} \underline{x}_{r,k}$$

(6)

for the periodic system or for the invariant system

$$\underline{x}_{r,k+1} = A_r \underline{x}_{r,k} + B_r \underline{x}_{FM,k}$$
$$\underline{y}_k = C_r \underline{x}_{r,k}$$

(7)

Before forming the coupled model the two systems need to be converted into the same time domain. When the ROM of the periodic system is used the flight mechanics system is transformed into the discrete-time domain so that the monodromy matrix may be evaluated simply. However, the ensemble-averaged aerodynamic system is converted into the continuous-time domain. A variety of methods exist for converting discrete-time systems into the continuous-time [25]. For this model, a sampling-based inversion transformation is used [25, 26], allowing for an arbitrary CFD system to replace the UVLM. These transformations are shown in Equation (9).

$$\dot{\underline{x}}_{A,r} = A_{A,r} \underline{x}_{A,r} + B_{A,r} \underline{x}_{FM}$$
$$\underline{y}_A = C_{A,r} \underline{x}_{A,r}$$

(8)

$$A_{A,r} = \frac{ln(A_r)}{\Delta t} \qquad\qquad B_{A,r} = (A_r - I)^{-1} A_{A,r} B_r \qquad\qquad C_{A,r} = C_r \qquad (9)$$

Finally, considerations regarding the coordinate frame of reference for Equations (3) and (8) must be made to allow the equations to be coupled. The flight mechanics states $\underline{x}_{FM}$ and aerodynamic forces $\underline{y}_A$ are in general taken about the body axes of the aircraft, apart from (x, y, z) which denotes the CG position relative to the inertial frame and (ϕ, θ, ψ) which are the Euler angles. Thus, we require the aerodynamic system inputs of $\underline{x}_{FM}$ and outputs of $\underline{y}_A$ to be transformed via the transformations in Equation (10).

$$\underline{y}_A\Big|_{aero} = R\underline{y}_A\Big|_{body} \qquad (10a) \qquad\qquad \underline{x}_{FM}\Big|_{aero} = L\underline{x}_{FM}\Big|_{body} \qquad (10b)$$

Now using Equations (3), (8) and (10) the resulting model for use in the tiltrotor stability analysis is given by Equation (11). The stability of the LTI system is given by the eigenvalues of the system matrix of this state-space equation, and the eigenvectors give the corresponding mode shapes. The eigenvectors will be of the form $[\underline{x}_{FM}^T, \underline{x}_{A,r}^T]^T$ and in combination with the associated eigenvalue allow one to reconstruct the time-history of the motion, be it the physical motion of the mode given by the $\underline{x}_{FM}$ states, or the (reduced) aerodynamic solutions given by the $\underline{x}_{A,r}$, which

6

require some extra considerations derived in Section III.C to reconstruct the full aerodynamic solution given by the $\underline{x}_A$ states.

$$\begin{bmatrix} \dot{\underline{x}}_{FM} \\ \dot{\underline{x}}_{A,r} \end{bmatrix} = \begin{bmatrix} \boldsymbol{A}_{FM} & \boldsymbol{E}_{FM}\boldsymbol{R}^{-1}\boldsymbol{C}_{A,r} \\ \boldsymbol{B}_{A,r}\boldsymbol{L} & \boldsymbol{A}_{A,r} \end{bmatrix} \begin{bmatrix} \underline{x}_{FM} \\ \underline{x}_{A,r} \end{bmatrix} \tag{11}$$

The trim response of the UVLM system is periodic with respect to the blade passing frequency of the proprotors (20 timesteps, see Section II.D). The solution is steady in the sense that the wake is fully developed and the mean value of the force response is unchanging, however the periodicity of the trim implies a non-linear limit cycle equilibrium. Because of this, an ensemble-averaging method has been implemented in order to eliminate the periodicity in the system, which effectively implies that the proprotors are treated as continuous discs as opposed to discrete blades. It should be noted that this actually aligns better with the representation of the flight mechanics of the tiltrotor used in this work, and the treatment of rotor dynamics as rigid spinning discs.

As per Guckenheimer and Holmes [27], we consider small perturbations of the linear system $\underline{\dot{x}} = \epsilon f(\underline{x}, t, \epsilon)$ where $0 \leq \epsilon << 1$ and the function f is periodic with period T. For slowly evolving ensemble-averaged solutions, one can form the associated ensemble-averaged system, denoted by $\underline{\dot{y}}$, in Equation (12). This equation is used to form the equivalent steady-state response from a sequence of impulse responses over the 20 timestep period of the UVLM system. This method aims to provide a much more computationally efficient method of analysis of such periodic systems. It should be noted that further investigation is required to ensure the equivalence of the ensemble-averaging and periodic system treatment. Regardless of this however, the ensemble-average still provides a more valid treatment of the periodic system than classical stability analysis.

$$\underline{\dot{y}} = \epsilon \frac{1}{T} \int_0^T \underline{f}(\underline{y}, t, 0) dt \stackrel{\text{def}}{=} \epsilon \underline{\overline{f}}(\underline{y}) \tag{12}$$

D. XV-15 Model Parameters and Construction

The XV-15 parameters used in this work have primarily been derived from the XV-15 Familiarisation Document [16], and cross-referenced with the model constructed by Kleinhesselink [15] to ensure that it remains similar to literature [14, 15, 28]. For instance for proprotor twist, a linear approximation to the true twist of the XV-15 proprotors was used as per [15]. Some parameters such as aircraft mass have been based upon literature and subsequently varied slightly to satisfy the trim condition, and all parameters have been taken for the XV-15 in helicopter mode. The parameters used to construct the flight mechanics of the XV-15 are listed in Table 1. For the UVLM model a simple cruciform flat-plate with image plane protruding from the underside was used to represent the projected area of the XV-15 airframe, with the inboard flaps and outboard flaperons deflected fully, a method to reduce wing download in the XV-15 operating in helicopter mode [16]. The two proprotors have been represented by blades consisting of twisted flat plates, and all bound vortex panel distributions are linear except

Fig. 4 UVLM mesh for the cruciform XV-15 aerodynamic model.

for the spanwise wing distribution, which is a cosine distribution with a tip offset to prevent excessive panelling at the wing tip. Key parameters used to construct this model can be seen in Table 2 and the resulting model is visualised in Figure 4.
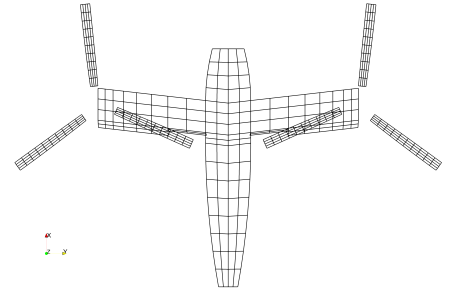
Table 1   XV-15 Aircraft Flight Mechanics Parameters

Parameter	Value	Unit	Parameter	Value	Unit
Gravity g	9.81	ms^{-2}	Inertia Component I_{xx}	71587.17	kgm^2
Mass m	5894.27	kg	Inertia Component I_{yy}	28960.27	kgm^2
Proprotor Disc Inertia I_d	416.91	kgm^2	Inertia Component I_{zz}	89944.94	kgm^2
Rotor Speed Ω	589.00	RPM	Inertia Component I_{xz}	1673.08	kgm^2

Table 2   XV-15 Aircraft UVLM and Panelling Parameters

Parameter	Value	Unit	Parameter	Value	Unit
	Wing			Fuselage	
Wing Chord	1.6002	m	Cabin Width aft	0.7250	m
Wing Span	9.8054	m	Cabin Length aft	5.2999	m
Wing Sweep	6.5000	deg	Cabin Width under Wing	1.7000	m
Wing Taper Ratio	1.0000	-	Cabin Length under Wing	1.6002	m
Wing Dihedral	2.0000	deg	Cabin Width forward	1.2000	m
Inboard Flap Hinge Length	1.2954	m	Cabin Length forward	2.0384	m
Outboard Flaperon Hinge Length	2.3957	m	Cabin Image Plane Length	3.6386	m
Flap/Flaperon Chord Fraction	0.2500	-	Cabin Image Plane Height	1.8796	m
Inboard Flap Deflection	75.0000	deg			
Outboard Flaperon Deflection	47.0000	deg			
	Rotor			Panelling	
Number of Blades	3	-	Blade Chordwise Panels	4	-
Rotor Radius	3.8100	m	Blade Spanwise Panels	10	-
Blade Chord	0.3556	m	Cabin Chordwise Panels aft	8	-
Linear Twist at Tip (tip down)	41.0000	deg	Cabin Chordwise Panels forward	4	-
Blade Angle at Hub	37.4256	deg	Cabin Spanwise Panels at Wing	4	-
Root Cutout Radius	0.7112	m	Wing Chordwise Panels	3	-
			Flap/Flaperon Chordwise Panels	2	-
	Other Run Parameters		Image Plane Height-Wise Panels	3	-
			Wing Spanwise Panels	8	-
Timestep Size	0.001698	s	Flap Spanwise Panels	2	-
Density	1.2389	$kg m^{-3}$	Flaperon Spanwise Panels	6	-
Maximum Wake Panels	180	-	Wing Tip Cosine Offset	0.3648	m
Maximum Wake Particles	14400	-			

Firstly, trim solution was formed for the aerodynamic model by converging the UVLM solution to a periodic steady-state in both the force response and the wake solutions. One can see from the process by which the UVLM works in Section II.B that the number of particles in the wake swells over time. This increases the size of the system to be solved thus vastly increasing computational cost of each timestep in the order of $O(n^2)$ where n is the number of particles. For this reason, and to encourage the system to converge to a steady-state in a reasonable amount of time, particles are only permitted to survive for a certain amount of time in the wake, which sets a limit on the maximum number of particles in the system at any time. It is necessary for the particles to convect far enough away from the airframe before being removed in order to have a sufficiently large wake model which approximates the full wake. This work has found that 240 timesteps of wake history (equivalent to 14400 particles here) gives sufficient convection of the wake away from the XV-15 wings by triple the distance between proprotor and the wing, equivalent in time to four revolutions of the proprotors. Four revolutions allows for suitable length time histories (at least for these preliminary investigations) of impulse response to be contained within the wake before getting removed, and allows the ROM to better identify the behaviour of the wake to such impulse responses. With the steady-state converged, an iterative process was used to trim the UVLM model. This involved varying the collective pitch of the proprotors until the vertical force was in equilibrium. The body axes, i.e. CG position, were then located at a position along the length (along the axis x_b) of the fuselage which provided zero net pitching moment. The other loads in $\underline{y}_A$ were found to be zero at steady-state by default due to the $x_b - z_b$ symmetry of the aircraft. This trim solution was then used as a base upon which to apply impulse perturbations for ROM identification. A visual representation of this steady-state aerodynamic system coloured by magnitude of induced velocity can be seen in Figure 5, and Figure 5b shows the representative steady-state force behaviour (shown for Z, but the other loads also show very similar behaviour to this).

It can be seen that the model does not explicitly capture a fountain flow effect via the vortex particles, however upon closer inspection of the port proprotor it can be observed that there is a slight upwash of the particles (and thus a small region of upwash in the velocity field) close to the region one would expect to find fountain flow. Unfortunately this is
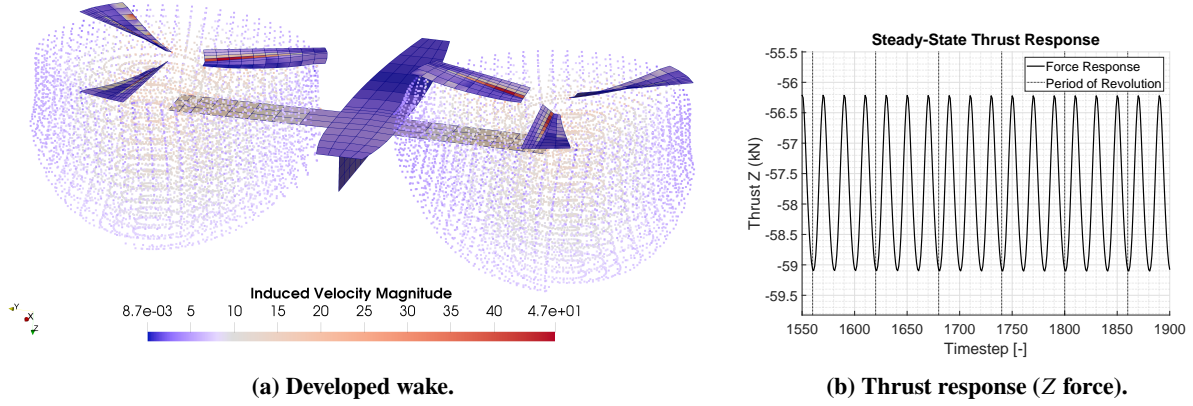
(a) Developed wake.

(b) Thrust response (Z force).

Fig. 5 UVLM system converged to a steady-state, trimmed solution

not seen on the starboard rotor due to the numerical linear equation solver implemented in the UVLM code, which leads to a slight asymmetry between the rotors. Indeed, one would expect the fountain flow to become more developed if the wake size was expanded, alongside an increase in the density of panelling on the wing to prevent non-physical errors due to particles getting drawn through the wing panels when in close proximity. Implementing a particle deflection scheme to the code for when particles enter a region defined to be a solid body is strongly recommended for future work, as this effect is also a source of numerical noise which effects the ERA (though the periodic ROM seems unaffected).

To form the ROM a set of Single-Input Multiple-Output (SIMO) system responses, due to an impulse at timesteps 1550 to 1569, is used. These impulses must be small enough size to provide a linear response about the trim condition such that the ROMs accurately model the linear behaviour of the UVLM without errors introduced by non-linear effects of a large pulse. For this work it was found that the input vector defined by Table 3, although implemented in a SIMO sense not MIMO, gave a linear impulse response about the trim condition. For the averaged ROM, the ensemble-averaged impulse response of the UVLM system from the non-linear trim condition via Equation (12) is needed. Here this is done by effectively determining a set of Single-Input Multiple-Output (SIMO) system responses due to an impulse at timesteps 1550 to 1569, shifted and averaged about timestep 1550 (i.e. forming the ensemble-average about the 20 timestep period seen in Figure 5b) in each of the $\underline{x}_{FM}$ inputs in order to form the Markov parameters Equation (15) required to form the ERA Hankel matrices.

Table 3 Sizes of impulses that give a linear UVLM impulse response about trim condition.

Pulse Variable	x	y	z	u	v	w	ϕ	θ	ψ	p	q	r
Pulse Size	0.0125	0.0125	0.05	0.1	0.1	0.1	1	1	1	0.1	0.1	0.1
Unit	m	m	m	ms^{-1}	ms^{-1}	ms^{-1}	$^{\circ}$	$^{\circ}$	$^{\circ}$	$^{\circ}s^{-1}$	$^{\circ}s^{-1}$	$^{\circ}s^{-1}$

III. Aerodynamic Model Order Reduction

This work investigates the use of both LTI and LTP model reduction for the analysis of coupled flight mechanics stability. ROMs have been previously used successfully to model aerodynamic systems [29]. This model order reduction can be done by identifying the most controllable and observable modes from the state-space model and only considering these to define the stability of the system. The ERA method is included for completeness before the new periodic ROM is developed. This new ROM methodology can be seen as the periodic system extension of ERA. Also outlined in this section is the reconstruction of the flowfield solution from the ROM and the pulses used in the model construction. The reconstruction is outlined for the ensemble averaged ROM only. A similar methodology can be followed for the periodic ROM but is not presented here as it has not yet been implemented.

A. Reduced Order Modelling and the Eigensystem Realisation Algorithm for LTI Systems

At their core, ROMs are simply the transformation of a system from its original basis onto a basis in which some states are negligible or redundant, and as such can be truncated with minimal loss in accuracy. In general the model reduction of the discrete LTI state-space system (A, B, C) via the non-singular transformation matrices T and S ($TS = I$) is performed as per Equation (13). Noting firstly that $\underline{x}_k = T\underline{x}_{r,k}$ where $\underline{x}_k$ is the original state vector and $\underline{x}_{r,k}$ the reduced state vector.

$$\underline{x}_{r,k+1} = SAT\underline{x}_{r,k} + SB\underline{u}_k$$
$$\underline{y}_k = CT\underline{x}_{r,k}$$

(13)

A concept often tied in with the formation of ROMs is that of balanced reductions, or balanced realisations. Effectively, a balanced reduction of a system implies that T and S are defined by the process of transforming the system in a way that balances the observability and controllability (or reachability) of each state. This balancing ensures that seemingly low-energy modes that may actually have a disproportionally large impact on the the system dynamics are not truncated due to being low-energy. This requires the condition $\Sigma = P = Q$ where P and Q are the controllability and observability gramians (of the reduced system) respectively.

Various methods of forming ROMs exist [30], such as the snapshot POD method, the Balanced snapshot POD method (BPOD) and the ERA. Snapshot POD (referred to as simply POD from here onwards) is by far the most common method in fluid dynamics [31, 32], due to both its maturity in fields such as aeroelastics and also the fact that it provides an optimal projection of the system onto a reduced basis with respect to captured energy [33]. However, POD does not result in a balanced system, and as such can result in the loss of important dynamic behaviour. BPOD provides a remedy to this by using information from the adjoint system stored in the discrete observability matrix, F, to represent the observability gramian ($Q = F^T F$) of the system. Along with the controllability gramian of the system ($P = GG^T$) formed from information from the nominal system, these can be utilised to form a balanced reduction. The transformations used in BPOD are defined in terms of the normal modes, $\underline{\phi}_r$ and the adjoint modes $\underline{\psi}_r$:

$$T = \begin{bmatrix} \underline{\phi}_1 & \cdots & \underline{\phi}_r \end{bmatrix} \qquad S = \begin{bmatrix} \underline{\psi}_1^* \\ \vdots \\ \underline{\psi}_r^* \end{bmatrix}$$

(14)

where here the $(\cdot)^*$ represents the transpose. The obvious drawback to this method, however, is the need to compute the solution to the adjoint system in parallel with the solution to the nominal system. Not only does this require extensive coding effort, but also it uses significantly more computational resources. In fact, both POD and BPOD require extensive modification to the source code of the CFD method if desired to be implemented.

The ERA has its origins as a system identification technique in civil engineering applications [34]. However, relatively recently its capability in producing ROMs for aerodynamics problems has started to be realised [35]. The ERA works by analysing the output of the impulse response of a system and using this to identify reduced (A_r, B_r, C_r) matrices without requiring computation or storage of POD modes (normal or adjoint) or any of the full system matrices. To form a ROM via the ERA, the Markov parameters Y_k of the discrete system (A, B, C) must be formed for $m + 1$ timesteps, which are the system's unit impulse response and are shown in Equation (15).

$$\begin{bmatrix} Y_1 & Y_2 & \ldots & Y_{m+1} \end{bmatrix} = \begin{bmatrix} CB & CAB & CA^2B & \ldots & CA^mB \end{bmatrix}$$

(15)

These Markov parameters are used to form a Hankel matrix H_1 and a shifted Hankel matrix H_2

$$H_1 = \begin{bmatrix} Y_0 & Y_1 & \cdots & Y_g \\ Y_1 & Y_2 & \cdots & Y_{g+1} \\ \vdots & \vdots & \ddots & \vdots \\ Y_s & Y_{s+1} & \cdots & Y_{m-1} \end{bmatrix} \quad H_2 = \begin{bmatrix} Y_1 & Y_2 & \cdots & Y_{g+1} \\ Y_2 & Y_3 & \cdots & Y_{g+2} \\ \vdots & \vdots & \ddots & \vdots \\ Y_{s+1} & Y_{s+2} & \cdots & Y_m \end{bmatrix}$$

(16)

The singular value decomposition of the Hankel matrix produces

$$\begin{bmatrix} H_r \\ H_o \end{bmatrix} = \begin{bmatrix} U_r & U_o \end{bmatrix} \begin{bmatrix} \Sigma_r & 0 \\ 0 & \Sigma_o \end{bmatrix} \begin{bmatrix} V_r \\ V_o \end{bmatrix}$$

(17)

and the reduced system is constructed using:

$$A_r = \Sigma_r^{\frac{1}{2}} U_r^T H_2 V_r \Sigma_r^{-\frac{1}{2}}$$

$$B_r = \underbrace{\Sigma_r^{\frac{1}{2}} V_r^T}_{\text{first } p \text{ columns}}$$

$$C_r = \underbrace{U_r \Sigma_r^{\frac{1}{2}}}_{\text{first } q \text{ rows}}$$

(18)

This method will be used to obtain a ROM of the ensemble averaged rotor aerodynamic response. However, whilst this may prove useful for the slow dynamics of the system we must also analyse the full periodic system.

B. Periodic ROM construction

In order to analyse the stability of linear time-varying dynamic systems it is necessary to obtain the state transition matrix. This models the change in the system dynamics between different instants in time. For two instants in time, i and j, the state transition matrix from time i to time j is defined as: $\Phi_A(j,i) = A_{j-1} A_{j-2} \cdots A_i$. For the case of a periodic system with period K, the state transition matrix over one period $\Phi_A(j+K, j)$ is referred to as the *monodromy matrix*. The stability of a periodic motion can therefore be represented by the eigenvalues of this monodromy matrix $\Lambda(\Phi_A(j+K, j))$, also referred to as *characteristic multipliers*. This is equivalent to finding the Poincaré map of a periodic motion as shown in Figure 6, where the successive intersections of the periodic orbit M with the plane S give the characteristic multipliers of the periodic motion. The system will be stable if all the characteristic multipliers are within the unit disk in the complex plane. [36, 37]. The problem therefore becomes the identification of the monodromy matrix for the coupled aerodynamics-flight mechanics tiltrotor system.
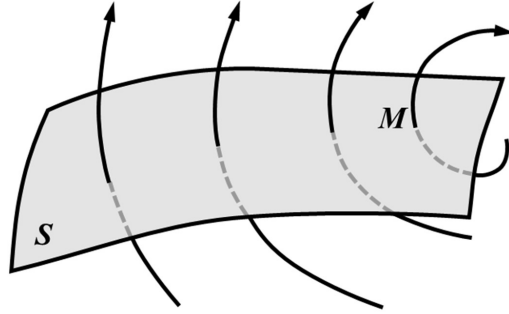

Fig. 6   Poincaré representation of periodic orbit.

Typically periodic systems have been analysed using a lifted-system approach, such as [38–41]. This is done by sampling the period K at k instants in time to form a time-invariant equivalent of the time-varying system, then analysing it using a standard representation. However, this can lead to very computationally expensive and complicated systems, and more recent work, particularly by Varga, has focused on obtaining balanced realisations of periodic systems, which would decrease computational expense [36, 42].

The method developed in this paper starts from the work of Varga [36], where a balancing realisation of a periodic system is computed by solving the Positive Discrete Periodic Lyapunov Equations (PDPLEs). However, the method presented avoids this numerically stiff calculation by approximating the gramians over a finite time history.

Two important definitions introduced in his work are the periodic reachability (refered to here as controllability) and observability gramians. Given the infinite columns matrix G_k and infinite rows matrix F_k at time k in Equations 19 and 20:

$$G_k = \begin{bmatrix} B_{k-1} & A_{k-1} B_{k-2} & \cdots & \Phi_A(k, i+1) B_i & \cdots \end{bmatrix}$$

(19)

$$F_k = \begin{bmatrix} C_k \\ C_{k+1}A_k \\ \vdots \\ C_i \Phi_A(i,k) \\ \vdots \end{bmatrix} \tag{20}$$

the infinite controllability and observability gramians at time k are then defined as:

$$P_k = G_k G_k^T = \sum_{i=-\infty}^{k-1} \Phi_A(k, i+1) B_i B_i^T \Phi_A(k, i+1)^T \geq 0$$

$$Q_k = F_k^T F_k = \sum_{i=k}^{\infty} \Phi_A(i,k)^T C_i^T C_i \Phi_A(i,k) \geq 0 \tag{21}$$

In this work finite gramians with a window of size m are used as approximations to the infinite gramians, such that

$$\tilde{G}_k = \begin{bmatrix} B_{k-1} & A_{k-1}B_{k-2} & \cdots & \Phi_A(k, k-m+1)B_{k-m} \end{bmatrix} \tag{22}$$

$$\tilde{F}_k = \begin{bmatrix} C_k \\ C_{k+1}A_k \\ \vdots \\ C_{k+m-1}\Phi_A(k+m-1,k) \end{bmatrix} \tag{23}$$

$$\tilde{P}_k = \tilde{G}_k \tilde{G}_k^T = \sum_{i=k-m}^{k-1} \Phi_A(k, i+1) B_i B_i^T \Phi_A(k, i+1)^T$$

$$\tilde{Q}_k = \tilde{F}_k^T \tilde{F}_k = \sum_{i=k}^{k+m-1} \Phi_A(i,k)^T C_i^T C_i \Phi_A(i,k) \tag{24}$$

The method proposed by Varga obtains a balanced minimal realisation of the periodic system by taking the Cholesky factorisation of the periodic controllability and observability gramians. An SVD of the product of the cholesky factors is then used to produce a Lyapunov similarity transform that balances the infinite gramians. Here, the finite cross gramian at each time step

$$\tilde{F}_k \tilde{G}_k = \begin{bmatrix} C_k B_{k-1} & \cdots & C_k \Phi_A(k, k-m+1)B_{k-m} \\ \vdots & \ddots & \vdots \\ C_{k+m-1}\Phi_A(k+m-1,k)B_{k-1} & \cdots & C_{k+m-1}\Phi_A(k+m-1,k)\Phi_A(k, k-m+1)B_{k-m} \end{bmatrix} \tag{25}$$

replaces the product of cholesky factors used by Varga. The finite cross gramians, at each timestep, correspond to sections of the system output response to pulses applied at each of the timesteps around the period. The SVD of the finite cross gramian

$$\tilde{F}_k \tilde{G}_k = U_k \Sigma_k V_k^T \tag{26}$$

can be used to form the balancing transform

$$T_k = \tilde{G}_k V_k \Sigma_k^{-1/2} \qquad S_k = \Sigma_k^{-1/2} U_k^T \tilde{F}_k \qquad S_k T_k = I \tag{27}$$

whose application within a periodic system will now be outlined.

Since we are working with periodic systems, a script notation is introduced to express the K periodic block diagonal matrices: $\mathscr{X} = diag(\tilde{X}_0, \tilde{X}_1 \ldots \tilde{X}_{K-1})$, as well as the K-cyclic shift: $\sigma \mathscr{X} = diag(\tilde{X}_1, \ldots, \tilde{X}_{k-1}, \tilde{X}_0)$. With this notation, two equivalent periodic systems can be related via the Lyapunov similarity transform

$$\left(\hat{\mathscr{A}}, \hat{\mathscr{B}}, \hat{\mathscr{C}}\right) = (\sigma \mathscr{S} \mathscr{A} \mathscr{T}, \sigma \mathscr{S} \mathscr{B}, \mathscr{C} \mathscr{T}) \qquad \mathscr{S} \mathscr{T} = \mathscr{I} \tag{28}$$

Both the infinite and finite gramians of this transformed system now satisfy

$$\hat{\mathscr{P}} = \mathscr{S} \mathscr{P} \mathscr{S} \quad , \qquad \hat{\mathscr{Q}} = \mathscr{T} \mathscr{Q} \mathscr{T} \tag{29}$$

The balancing transform, written in the periodic script notation becomes

$$\mathscr{T} = \mathscr{G} \mathscr{V} \mathscr{E}^{-1/2} \quad , \qquad \mathscr{S} = \mathscr{E}^{-1/2} \mathscr{U}^T \mathscr{F} \tag{30}$$

where $\mathscr{E} = diag(\Sigma_0, \Sigma_1 \ldots \Sigma_{K-1})$. It is relatively straightforward to show, see appendix C, that this transform balances the gramians, i.e.

$$\mathscr{P} = \mathscr{Q} = \mathscr{E} \tag{31}$$

Just as in the application of ERA to LTI systems, reduced systems of dimension r can be formed for each time step by taking the leading terms of the balancing transform such that

$$\tilde{F}_k \tilde{G}_k = \begin{bmatrix} U_{r,k} & U_{0,k} \end{bmatrix} \begin{bmatrix} \Sigma_{r,k} & 0 \\ 0 & \Sigma_{0,k} \end{bmatrix} \begin{bmatrix} V_{r,k} \\ V_{0,k} \end{bmatrix} \tag{32}$$

and

$$T_{r,k} = \tilde{G}_k V_{r,k} \Sigma_{r,k}^{-1/2} \qquad S_{r,k} = \Sigma_{r,k}^{-1/2} U_{r,k}^T \tilde{F}_k \tag{33}$$

From this, it can be seen that a new approach to produce periodic ROMs can be presented. This method will compute an approximately balanced model order reduction but will not require the computation of the PDPLEs .

1) Calculate the pulse response, of length $2m - 1$, at each of the K timesteps around the period
2) Form the finite cross gramian for each timestep in the period
3) Perform the SVD of the cross gramian for each timestep: $\tilde{F}_k \tilde{G}_k = U_k \Sigma_k V_k^T$,.
4) Obtain transformation matrices at each timestep: $T_{r,k} = \tilde{G}_k V_{r,k} \Sigma_{r,k}^{-1/2}$ and $S_{r,k} = \Sigma_{r,k}^{-1/2} U_{r,k}^T \tilde{F}_k$.
5) Calculate the reduced system $(\mathscr{A}_r, \mathscr{B}_r, \mathscr{C}_r)$ is as per Equation 28: $(\sigma \mathscr{S}_r \mathscr{A} \mathscr{T}_r, \sigma \mathscr{S}_r \mathscr{B}, \mathscr{C} \mathscr{T}_r)$

Writing the reduction in this form is important as it highlights the relationship with an equivalent balanced periodic POD. A balanced periodic POD methodology is produced in [43] which would be equivalent to the method presented here, except that a lifting approach was taken rather than using the Lyapunov similarity transform. It can be seen that for a balanced POD equivalent to our method, new sets of normal and adjoint modes would be constructed for each time step. Indeed, the adjoint modes would project the solution, in terms of the basis used at one timestep, onto the basis used for the next timestep. Whilst this is interesting, our new method can be streamlined and the requirement for construction of the original matrices removed as follows.

Firstly, by considering the calculation of the reduced system matrix at timestep k, $A_{r,k}$, we can see that

$$\begin{aligned} A_{r,k} &= \sigma \left(\Sigma_{r,k}^{-1/2} U_{r,k}^T \tilde{F}_k \right) A_k \left(\tilde{G}_k V_{r,k} \Sigma_{r,k}^{-1/2} \right) \\ &= \left(\Sigma_{r,k+1}^{-1/2} U_{r,k+1}^T \right) \tilde{F}_{k+1} A_k \tilde{G}_k \left(V_{r,k} \Sigma_{r,k}^{-1/2} \right) \end{aligned} \tag{34}$$

which can be written in terms of a matrix that represents the cross gramian shifted by one time step, $\left(\tilde{F}_k \tilde{G}_k \right)_+$, i.e.:

$$A_{r,k} = \left(\Sigma_{r,k+1}^{-1/2} U_{r,k+1}^T \right) \left(\tilde{F}_k \tilde{G}_k \right)_+ \left(V_{r,k} \Sigma_{r,k}^{-1/2} \right) \tag{35}$$

Therefore the system matrix $A_{r,k}$ can be calculated by simply taking an additional timestep of the system response to each pulse.

13

Secondly, considering the calculation of the reduced input matrix at timestep k, $B_{r,k}$, we can see that

$$B_{r,k} = \Sigma_{r,k+1}^{-1/2} U_{r,k+1}^T \tilde{F}_{k+1} B_k$$

$$= \Sigma_{r,k+1}^{-1/2} U_{r,k+1}^T \begin{bmatrix} C_{k+1}B_k \\ \vdots \\ C_{k+m}\Phi_A(k+m,k)B_k \end{bmatrix} = \underbrace{\Sigma_{r,k+1}^{-1/2} U_{r,k+1}^T \tilde{F}_{k+1} \tilde{G}_{k+1}}_{\text{first p columns}} \tag{36}$$

$$= \underbrace{\Sigma_{r,k+1}^{-1/2} U_{r,k+1}^T U_{k+1}\Sigma_{k+1}V_{k+1}^T}_{\text{first p columns}} = \underbrace{\Sigma_{r,k+1}^{1/2} V_{r,k+1}^T}_{\text{first p columns}}$$

and similarly for the output matrix at timestep k, $C_{r,k}$,

$$C_{r,k} = C_k \tilde{G}_k V_{r,k} \Sigma_{r,k}^{-1/2}$$

$$= \begin{bmatrix} C_k B_{k-1} & \cdots & C_k \Phi_A(k,k-m)B_{k-m} \end{bmatrix} V_{r,k}\Sigma_{r,k}^{-1/2} = \underbrace{\tilde{F}_k \tilde{G}_k V_{r,k}\Sigma_{r,k}^{-1/2}}_{\text{first q rows}} \tag{37}$$

$$= \underbrace{U_k \Sigma_k V_k^T V_{r,k}\Sigma_{r,k}^{-1/2}}_{\text{first q rows}} = \underbrace{U_{r,k}\Sigma_{r,k}^{1/2}}_{\text{first q rows}}$$

This gives a very similar result to that obtained for the reduced B and C matrices using the ERA method. Hence the new approach to produce periodic ROMs can be presented which only requires the evaluation of the system pulse responses. It would also seem that, like ERA and its many variants, this method will have simple extensions to both realisation and experimental system identification.

1) Calculate the pulse response, of length $2m$, at each of the K timesteps around the period.
2) Form the finite cross gramians and their associated shifted forms, for each timestep in the period.
3) Perform the SVD of the finite cross gramian for each timestep: $\tilde{F}_k \tilde{G}_k = U_k \Sigma_k V_k^T$.
4) Calculate the reduced system

$$A_{r,k} = \left(\Sigma_{r,k+1}^{-1/2} U_{r,k+1}^T \right) \left(\tilde{F}_k \tilde{G}_k \right)_+ \left(V_{r,k}\Sigma_{r,k}^{-1/2} \right)$$

$$B_{r,k} = \underbrace{\Sigma_{r,k+1}^{1/2} V_{r,k+1}^T}_{\text{first p columns}} \tag{38}$$

$$C_{r,k} = \underbrace{U_{r,k}\Sigma_{r,k}^{1/2}}_{\text{first q rows}}$$

This reduced model can then be coupled with the flight mechanics and the monodromy matrix for the coupled system calculated.

C. POD Mode Reconstruction from Restarted ERA of the LTI System

Reconstruction of the normal POD modes (also referred to as the primal POD modes) from a ROM constructed via the ERA is relatively simple, and can be done by considering the equivalence of ERA and BPOD. An equivalence between BPOD and ERA can be readily shown by considering the following conditions:

1) The quadrature coefficients in G and F are neglected such that each coefficient equals unity. These coefficients normally denote the weighting of each state vector $\underline{x}_i(t_j)$ (the impulse response state due to impulse in input i at timestep of snapshot j) to the integrals defining the observability and controllability gramians respectively, and so neglecting simply constrains the snapshots to a constant Δt, and the effect of these coefficients would be a scaling factor applied to the gramians. This scaling corresponds to a uniform scaling of the singular values, thus not affecting either the accuracy of the ROM or the resulting system dynamics.

2) The snapshots in BPOD are formed via the same time integration technique as that in the ERA.
Thus we note some relations, where F and G are the discrete observability and controllability matrices, which can be found by analysing the discrete time $\underline{x}$ and $\underline{z}$ solutions of the discretised normal and adjoint systems respectively like so:

$$
\begin{aligned}
Z &= \left[\underline{z}_1(t_1), \underline{z}_2(t_1), \ldots, \underline{z}_q(t_1), \ldots \ldots, \underline{z}_1(t_{s+1}), \ldots, \underline{z}_q(t_{s+1})\right] \\
&= \left[C^T \quad A^T C^T \quad (A^T)^2 C^T \ldots (A^T)^s C^T\right] = F^T
\end{aligned}
\tag{39a}
$$

$$
\begin{aligned}
X &= \left[\underline{x}_1(t_1), \underline{x}_2(t_1), \ldots, \underline{x}_p(t_1), \ldots \ldots, \underline{x}_1(t_{g+1}), \ldots, \underline{x}_p(t_{g+1})\right] \\
&= \left[B \quad AB \quad A^2 B \ldots A^g B\right] = G
\end{aligned}
\tag{39b}
$$

Where $s + 1$ is the number of timesteps of the adjoint system time-history and $g + 1$ the number of timesteps of the normal system time-history. These correspond to the size of the Hankel matrix which is a block $(s + 1) \times (g + 1)$ matrix corresponding to $g + s + 1$ Markov parameters.

Equations (39a) and (39b) imply that the Singular Value Decomposition (SVD) applied to the Hankel matrix H_1 in the ERA is the same as the SVD applied to the $F^T G$ matrix product in BPOD.

Carried through the BPOD process of forming the normal and adjoint POD modes T and S, and truncating them to T_r and S_r respectively, where:

$$
\begin{aligned}
T_r &= XV_r \Sigma_r^{-1/2} \\
S_r &= \Sigma_r^{-1/2} U_r^T Z^T
\end{aligned}
\tag{40}
$$

Noting that U_r, Σ_r, V_r are from the truncation of the SVD of H_1, it can be readily shown that the ROM matrices A_r, B_r, C_r produced by the BPOD analysis are equivalent to those produced by the ERA.

This equivalence allows the extraction of normal POD modes from the ERA, allowing utilisation of the low computational cost of ERA (see Ma and Rowley [35] for comparisons) whilst retaining the ability to produce POD modes. These modes are very useful, and can be used for solution reconstruction as per this work, or could be applied alongside the adjoint modes to directly reduce the non-linear aerodynamic system. It should be noted that although attempts have been made to extract the adjoint modes from the ERA, this is still an active field of study as the systems produced are not balanced. A good example of such work can again be found in [35]. Here, an attempt was made to use the pseudo-inverse of T_r and construct the adjoint modes S_r via the bi-orthogonality relationship $S_r^T T_r = I_r$ as per Or and Speyer [44], however the resulting system is not balanced, and instead much more closely resembles the systems produced by snapshot POD so will not be discussed further.

Before extraction of the POD modes, the effect of restarting (and any numerical scaling) upon the system has to be considered. After the restarting process has been completed and a stable ROM obtained, we note that the Hankel H_1 matrix now contains the transformed matrix $\overline{B}$ as opposed B, such that $H_1 \to \overline{H}_1$ and hence throughout the above equations it can be seen that all B terms become $\overline{B}$ terms, related via:

$$
\overline{B} = \left(\prod_{j=1}^{n_t} \left(A - \mu_{(n_t+1-j)}I\right)\right) B
\tag{41}
$$

For solution reconstruction, noting that $X \to \overline{X}$ and that $\left(\prod_{j=1}^{n_t} \left(A - \mu_{(n_t+1-j)}I\right)\right)$ and A are commutative, Equation (39b) and Equation (42) give $\overline{X}$ in terms of the solution matrix X as:

$$
\overline{X} = \left[\overline{B} \quad A\overline{B} \quad A^2\overline{B} \ldots A^g \overline{B}\right] = \prod_{j=1}^{n_t} \left(A - \mu_{(n_t+1-j)}I\right) \left[B \quad AB \quad A^2 B \ldots A^g B\right]
$$

$$
\overline{X} = \prod_{j=1}^{n_t} \left(A - \mu_{(n_t+1-j)}I\right) X
\tag{42}
$$

As an example, using the case of a single real restart of μ_1 that acts to reduce the number of block rows in the restart-stabilised $\boldsymbol{H_1}$ matrix by one, expanding Equation (42) gives the following:

$$\overline{X} = (A - \mu_1 I)\, X = (AX - \mu_1 X)$$

We then define:

$$X_{a,b} = \begin{bmatrix} A^a B & A^{1+a} B \dots A^{g+a} B \dots A^{g+a+b} B \end{bmatrix} \tag{43}$$

Such that $X \equiv X_{0,0}$ to find that:

$$\overline{X} = \left(X_{1,0} - \mu_1 X_{0,0}\right) = X_{0,1} \begin{bmatrix} -\mu_1 I & 0 & \dots & 0 \\ I & -\mu_1 I & \ddots & \vdots \\ 0 & I & \ddots & 0 \\ \vdots & \ddots & \ddots & -\mu_1 I \\ 0 & \dots & 0 & I \end{bmatrix} = X_{0,1}\boldsymbol{\Theta} \tag{44}$$

Where $\boldsymbol{\Theta}$, referred to as the shift matrix, is of block size $(g + 2) \times (g + 1)$ for this case and the size of the blocks $\boldsymbol{I}$ are $p \times p$ where p is the number of inputs. Subsequently, for this case of the single real restart that acts to reduce $\boldsymbol{H_1}$ by one block row, the normal POD mode equation in Equation (40) becomes:

$$T_r = \overline{X} V_r \Sigma_r^{-1/2} = X_{0,1} \boldsymbol{\Theta} V_r \Sigma_r^{-1/2} \tag{45}$$

Where we note that the SVD terms in this equation are also now derived from $\overline{\boldsymbol{H}}_1$, i.e. the restart stabilised Hankel matrix that has had one block row removed (the first block row of the original $\boldsymbol{H_1}$) to accommodate the restart. We also note that the solution history required is now one term longer, i.e. one extra timestep needs to be stored.

Equation (45) and the above process generalises to an arbitrary number of complex and/or real restart combinations, and thus the generalised equation to form the POD modes from a restarted and pre-conditioned system is shown in Equation (46). The total number of shifts is given by $n_t = n_r + 2n_c$, where n_r are the number of real restarts and n_c are the number of complex restarts. The shift matrix for this general case can be formed (albeit not very efficiently, but good for visual aid) via Equation (47), where the matrix $\boldsymbol{\Theta}_1$ is the shift matrix for the first eigenvalue shift (either 1 real or 1 eigenvalue of the 2 of a complex shift) of the same form as that in Equation (44) but of block size $(g + \alpha + 1) \times (g - l + 1)$ with each block of size $p \times p$. The $\boldsymbol{\Theta}_i$ shift matrices are of block size $(g + \alpha + 1) \times (g + \alpha + 1)$ with each block being $p \times p$ and correspond to the shift matrix for the eigenvalue of shift i. Again, note that a complex restart is two eigenvalues, and thus two shifts.

Restarting is practically implemented by starting from as large a Hankel matrix as possible (i.e. using all available Markov parameters) and reducing the system size down with every restart. However, restarting is typically thought of with a constant-size system and an increasing number of Markov parameters required to define the Hankel matrices. This means that in the POD mode calculation, whether a row or column is removed from the Hankel matrix denotes whether the system size reducing or number of Markov parameters increasing is required to accommodate the restart. In Equations (46) and (47) this is taken into account via α and l. α denotes the total number of shifts that lead to a loss of a row from $\boldsymbol{H_1}$, an act that does not change the size of the SVD terms and so explicitly requires more blocks in X, and l denotes the total number of shifts that lead to a loss of a column from $\boldsymbol{H_1}$, an act that reduces the size of V_r and thus accommodates the restart by implicitly increasing the size of X *relative* to the system. $\boldsymbol{\Theta}$ is of block size $(g + \alpha + 1) \times (g - l + 1)$ (total size $(g + \alpha + 1)p \times (g - l + 1)p$), V_r is of size $(g - l + 1)p \times r$ and $\Sigma_r^{-0.5}$ is of size $r \times r$. r is the size of the reduced model.

$$\Phi_r = X_{0,\alpha} \boldsymbol{\Theta} V_r \Sigma_r^{-0.5} \tag{46}$$

$$\boldsymbol{\Theta} = \prod_{j=2}^{n_t} \boldsymbol{\Theta}_{(n_t+2-j)} \boldsymbol{\Theta}_1 \tag{47}$$

$$\underline{x} = \boldsymbol{T}_r \underline{x}_r \tag{48}$$

Thus, the POD modes are equal to a CFD component (the solution matrix $\boldsymbol{X}$ formed from impulse responses) multiplied by an ERA component, formed post-CFD during the ROM creation at much lower computational expense. This maintains the positive aspect of ERA in that it does not require code modification, and if modifications are made to the ROM (for example shifting eigenvalues) the POD modes can be re-formed readily without altering $\boldsymbol{X}$. Solution vectors for a point in time can then be reconstructed from the ROM states $\underline{x}_r$ and the POD modes $\boldsymbol{T}_r$ via Equation (48) for vastly reduced computational expense.

Of obvious detriment is the requirement to store this $\boldsymbol{X}$ matrix, and it should be noted that this may be no easy feat depending on the size of the CFD system. However, due to the structure of Equation (46), the solution vectors used to form the POD modes could contain only the solutions of interest and the POD modes would reflect this. For example, one could store only the solutions at the surface mesh for a RANS simulation without storing potentially millions of solution elements from the volume mesh, and use these to form the POD modes via Equation (46). Subsequently, the reconstructed solutions from Equation (48) would be reconstructions of these surface mesh solutions.

IV. Results

A. Validation of Averaged ROM Force Response and Solution Reconstruction

Before integrating the averaged ROM of the UVLM aerodynamics into the coupled model, it is first necessary to ensure that the ROM is indeed capable of reproducing both the force response and the solution history of the UVLM for an impulse in any of the flight mechanics states. It was found that a ROM of size 100 (i.e. 100 reduced aerodynamic states) without pre-conditioning or restarting applied gave good agreement with the UVLM response in general. This was for both the force response and the solution reconstruction to a small impulse in any $\underline{x}_{FM}$ state, equal to or smaller than those listed in Table 3. It is anticipated however that if the size of impulse given increases above these then accuracy will be lost due to non-linear effects not modelled by the ROM. This is especially true for the angular displacement or rate pulses, as for pulse sizes close to the limit of the small angle assumption non-linear effects will become prominent. Comparison of the UVLM and ERA output (force) responses for SIMO simulations in inputs x and r (of sizes as per Table 3) are shown in Figure 8 for the first 10 timesteps to visualise the ROM accuracy,

Fig. 7 **ROM failure at the low magnitude $[r, Z]$ pair due to noise.**

and a portion of the solution reconstruction for these pulses are shown in Figure 9. For the solution reconstruction validation, the solution targeted for validation was a measure of vorticity magnitude that has been averaged over a set of panels. For example, Figure 9a shows the average vorticity magnitude over the panels of the port wing at each timestep after the impulse in x. It should be noted that due to this being an ensemble-averaged analysis, the UVLM results for both force and solution validation have also been ensemble-averaged to provide a comparable validation case.

Whilst the responses shown in Figures 8 and 9 broadly show good agreement between the UVLM and ERA models of the aerodynamic system, it should be noted that for a few of the IO pairs that have low magnitude output responses, such as $[r, Z]$ seen in Figure 7, the noise power present in the response becomes larger in magnitude relative to the response itself. This causes the ERA to overfit the response in an effort to capture these noisy dynamics and thus creates a model that does not agree well with the true UVLM response. The effect of this is clear in Figure 7, where the initial transient over the first few timesteps is well modelled but the model quickly diverges from the true solution likely due to the noise present from timesteps 60 to 100. This noise is likely due to the particles traversing the distance between rotor and wing (approximately 80 timesteps of convection) and then sporadically being drawn through the wing panels slightly differently to how they would have if there had been no impulse, thus creating low-magnitude noise. This is an issue with the UVLM simulation mentioned previously in Section II.D, however it provides a useful insight into the sensitivity of the ERA to noisy data. Methods exist to reduce the influence of noise on the ERA [45], which could prove useful in future work utilising a noisier CFD code or experimental basis. However it is recommended for future work utilising the UVLM code to implement a particle deflection scheme to eliminate non-physical flow behaviour.
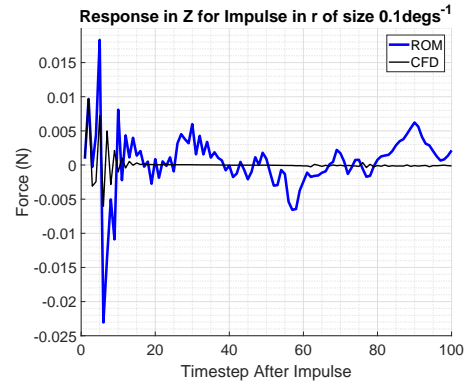
17

(a) Impulse in x.   **(b)** Impulse in r
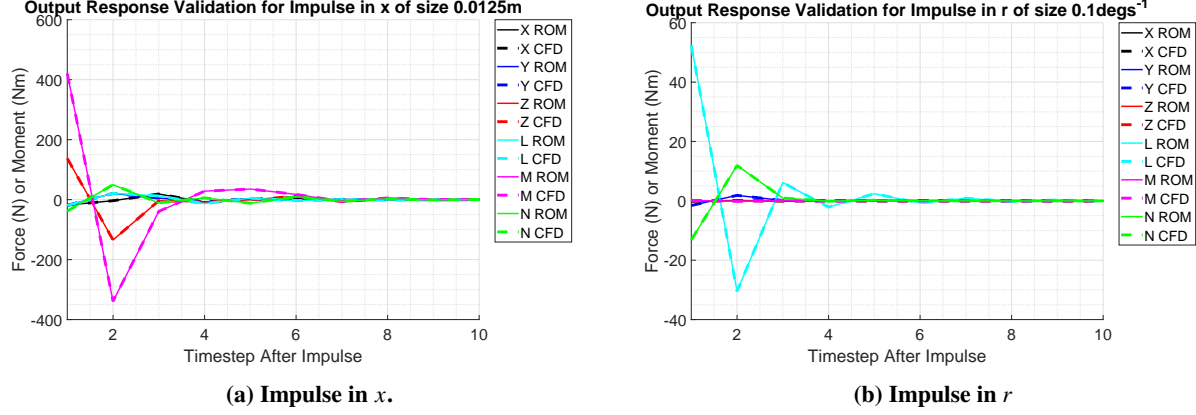
Fig. 8   Output response comparison between UVLM and ERA systems for SIMO impulses.

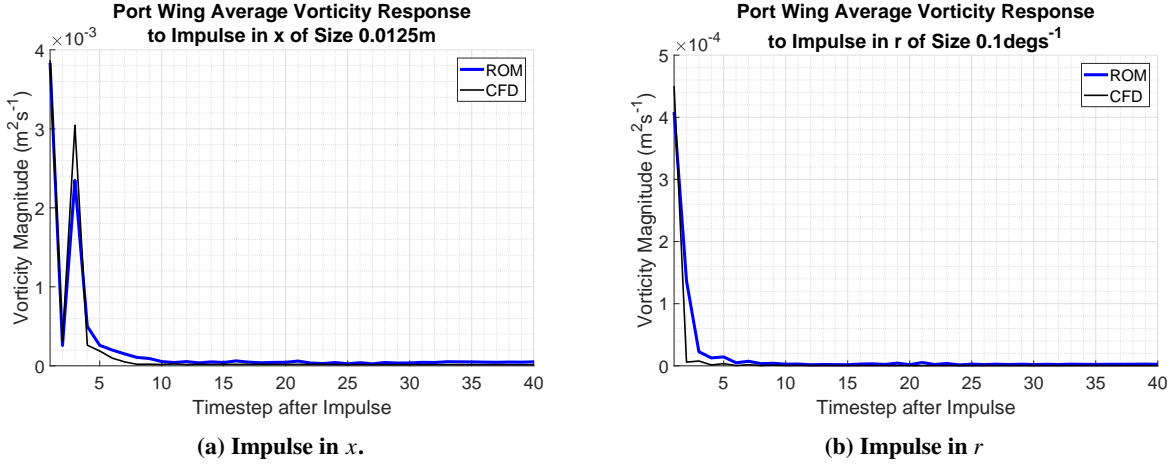**(a)** Impulse in x.   **(b)** Impulse in r

Fig. 9   Comparison of UVLM and ERA responses of average vorticity solution over port wing for SIMO impulses.

Decreasing ROM size, as expected, also reduces the accuracy of both the force and solution reconstructions, with the solution reconstruction tending to be more sensitive to a reduction in size. A ROM size of 100 was the optimum given the dataset provided, with the lower limit of ROM size being 50. At a size of 50 the largest magnitude IO pairs were still captured, however the smaller magnitude pairs started to diverge . Ideally future work should construct a larger UVLM impulse response time history in order to allow further increase in the model size. This would result in better accuracy for negligible change in computational expense. Future work would benefit from investigating alternative methods of ROM stabilisation that do not incur such a loss in accuracy, however it is also likely that the elimination of noise may result in a stable ROM by default.

In efforts to provide further insight into the accuracy of the ROM relative to the UVLM when dealing with a more complex input, the validation study was extended to compare the system responses when given a harmonic input, this applied to the z and w input channels. The amplitude of the cosine (z_{max}) was set to $0.00125m$ to prevent the velocity w from exceeding the linear size from Table 3 at any time. The effective period of the cosine (T) was set to 100 timesteps and Δt is given in Table 2.

$$z_k = \left(1 - cos\left(\frac{2\pi}{T}\right)\right) z_{max}$$

$$w_k = \frac{2\pi}{T\Delta t} sin\left(\frac{2\pi}{T}\right) z_{max}$$

$$(49)$$

The results show that, in general, the transient force response is modelled well by the ERA, and high-magnitude output responses such as pitching moment M and thrust Z are modelled exceptionally well in both the transient and long term responses (as before). However, low-magnitude output responses tend to be quite poorly modelled and in the case of the moment, N, the ERA seemingly fails to model the output response. The case of N is interesting, as intuitively one would assume that there would be zero response in yawing moment due to motions purely applied in the z_b direction because of the symmetry of the model about the x_b-z_b plane. This implies that it is likely that the asymmetry of the UVLM due to the numerical solver (as discussed in Section II.D) is having an impact on the aerodynamic modelling. Thus it is likely that the ERA is attempting to model non-physical aerodynamics, and so its failure to do so will have as large an effect on the model accuracy as the non-physical artefact does in the first place. This validation process for the thrust Z is visualised in Figure 10a. The solution reconstruction also shows encouraging behaviour, and in the case of the wing vorticities gives very close agreement. Again, the reconstruction of average vorticity magnitude over the panels of the port wing at each timestep can be seen in Figure 10b to highlight the general accuracy of the ERA.
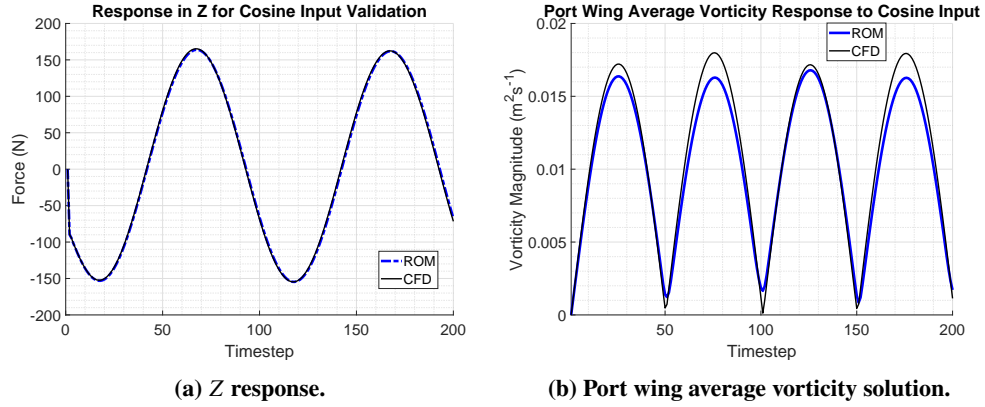

(a) Z response.

(b) Port wing average vorticity solution.

Fig. 10   Comparison of UVLM and ERA responses for force modelling and solution reconstruction with cosine input.

Noting the validation study above, investigations presented in the following sections utilise the size 100 ROM with no restarting applied.

B. Investigation into Tiltrotor Stability via the Averaged Coupled Model

(a) All eigenvalues.

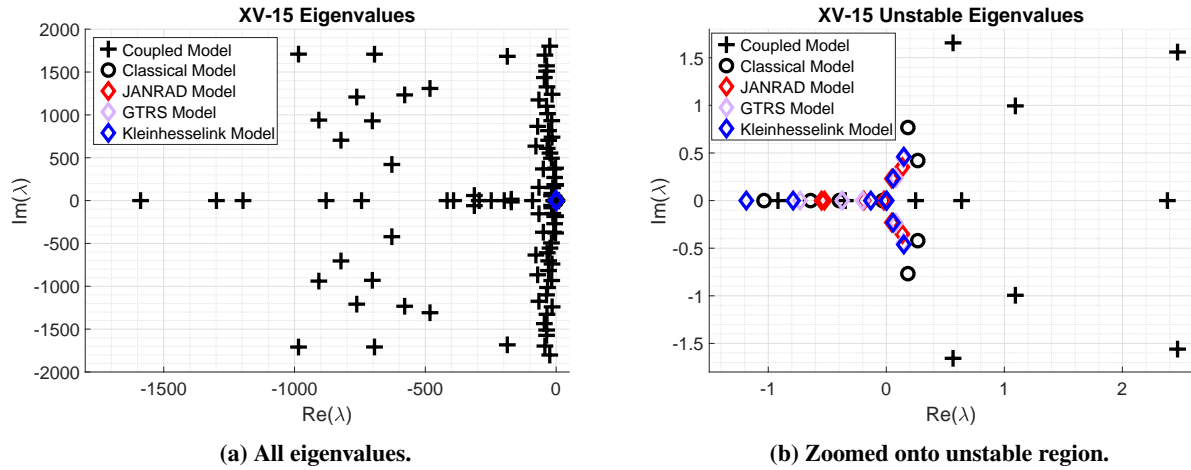(b) Zoomed onto unstable region.

Fig. 11   XV-15 stability predictions via the coupled model, the classical equivalent to the coupled model, and the three reference models: JANRAD [28], GTRS [14, 28] and Kleinhesselink [15].

The stability predictions for the XV-15 in hover given by the coupled model with the averaged ROM, equivalent

classical model, and three reference models can be seen in Figure 11, where large number of stable eigenvalues seen in Figure 11a effectively represent the ROM modelling of the aerodynamics, thus the plot of real interest for comparison is Figure 11b. The three reference models used were Kleinhesselink's development of a relatively simple tiltrotor model, uncorrected for flight data [15], the JANRAD model, which was developed from an adaptation of helicopter stability modelling code [28], and the GTRS model by NASA, which is heavily corrected with empirical data in an effort to correlate with flight data and as such is often considered in literature as a reference model for model development [14].

It can be seen from Figure 11b that the distribution of unstable eigenvalues has a similar shape between all models, except where the coupled model has one extra real and one extra complex pair of unstable eigenvalues. Also, in general the coupled model appears to predict eigenvalues that are significantly more unstable than those predicted by the references, or indeed the classical equivalent model. This is a fascinating result, as the coupled and classical models are based upon the same flight mechanics and aerodynamic system. The difference between them arises simply from the use of Taylor series about the steady aerodynamics. The effect of this is seen to be destabilising, however there is a possibility that numerical instabilities or dynamic 'quirks' present in the ROM have presented themselves as instabilities in the coupled model. However, the problem remains that currently there is not a method to know whether a numerical artefact in one of the systems has led to an instability in the coupled model.

C. Investigation of Flow Solution at Unstable Modes

Using the method developed in Section III.C the flow solution corresponding to an unstable motion can be reconstructed via the calculation of the POD modes of the system. These modes were constructed using Equation (46) in parallel with the formation of the ERA in Section II.D. With the POD modes formed, one can analyse Figure 11b, select the eigenvalue and corresponding eigenvector of interest, and then reconstruct the state vector of the coupled model $\underline{x}_c$, via $\underline{x}_c = w_i e^{\lambda_i t}$ for a real eigenvalue and $\underline{x}_c = w_i e^{\lambda_i t} + w_i^* e^{\lambda_i^* t}$ for a complex pair where w_i is the eigenvector and λ_i is the eigenvalue. Noting the formation of the coupled model in Equation (11) we note that $\underline{x}_c = \left[\underline{x}_{FM}^T, \underline{x}_{A,r}^T \right]^T$. Thus, the flight mechanics motion is implicitly calculated for visualisation of the mode shape, and the reduced aerodynamic states $\underline{x}_{A,r}$ can be used in $\underline{x}_A = T_r \underline{x}_{A,r}$ to reconstruct the aerodynamic solutions $\underline{x}_A$.

For an example of this process, the complex pair of eigenvalues at $\lambda_i = 0.57 \pm 1.66i$ has been investigated. Calculation of the flight mechanics states $\underline{x}_{FM}$ associated with this motion shows the instability to be a heaving motion in z_b coupled with a pitching motion about y_b. Feeding the reduced aerodynamic states $\underline{x}_{A,r}$ through the reconstruction to produce the aerodynamic solutions $\underline{x}_A$ for each timestep then allows a similar analysis of average vorticities as carried out in Section IV.A. Here, the average vorticities over the port wing panels and port rotor blade panels have been reconstructed to give an idea of the general aerodynamic response, and can be seen in Figure 12.

(a) Port wing.　　　　(b) Port rotor blades.
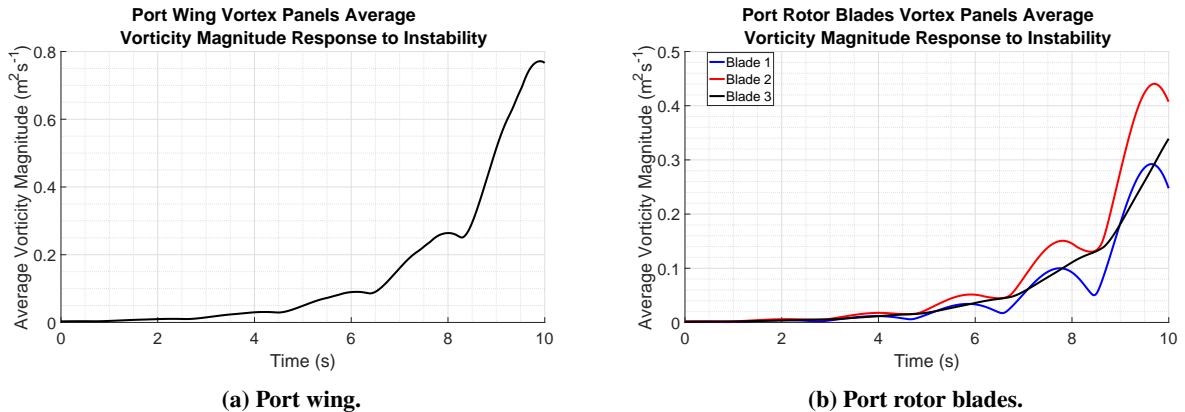
Fig. 12　Reconstruction of average port wing panel vorticity and average port rotor blade vorticity due to unstable motion of eigenvalue $\lambda_i = 0.57 \pm 1.66i$.

Whilst Figure 12 provides some insight into the instability, the POD modes formed actually contain the vorticity perturbation vectors for all wake particles, panels and bound panels, alongside their position perturbation vectors. Thus, much more detailed analysis can be performed by peering deeper into the solutions and selecting appropriate sets of data to analyse from this $\underline{x}_A$ solution vector. An example of this deeper investigation is given in Figure 13, which

shows the distribution of vorticity about the spanwise y_b axis over the leading edge panels of the port wing and its development over time due to the unstable motion. One can see from the plot that the wing tip (most negative y_b value due to this being the port wing) provides the most violent vorticity perturbation responses. This is likely due to the strong proprotor downwash that the wing tip operates in. The induced velocity produced by the port proprotor strongly influences the effective angle of incidence (and thus lift and vorticity) experienced by the wing, and the case may be that a destructive interaction exists where the flight mechanics states perturb the proprotor-wake induced velocity, which in turn perturbs the vorticity experienced at the wing tip, producing an output force/moment response that couples back into increasingly unstable flight mechanics states. This would align with the heaving/pitching motions seen to dominate the unstable motion. If this is indeed the case, then it could be possible from a design standpoint to implement an active lift destruction device such as a small spoiler at the wing tip in an effort to break the chain of destructive interaction and stabilise the motion.
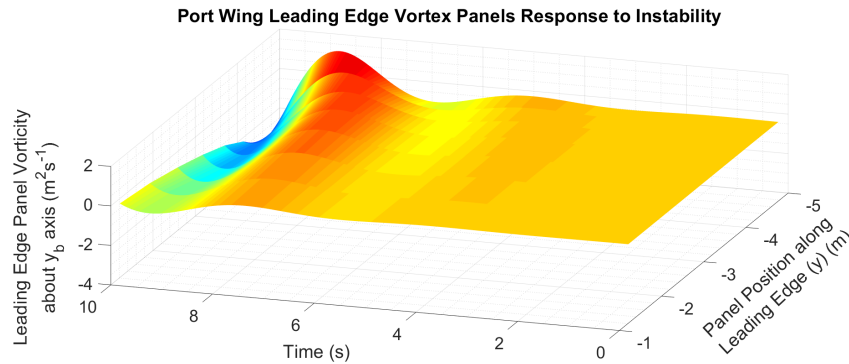

Fig. 13   Reconstruction of vorticity time history about axis y_b over the leading edge vortex panels of the port wing, due to unstable motion of eigenvalue $\lambda_i = 0.57 \pm 1.66i$.

This gives an encouraging example showcasing the potential for the coupled model to aid in the design of stability at a preliminary design level, and gives insight into the mechanism by which this process could work. Reconstructing this detailed solution history of approximately 25000 timesteps took in the order of 10 seconds to one minute to calculate. Currently, aircraft stability is typically treated as an analysis process post-design. However, with the rapid solution and force response reconstruction offered implicitly via stability analysis with a coupled model, it could be possible for stability to play a bigger role in the design process of both conventional and unconventional aircraft such as tiltrotors.

D. Coupled Stability Analysis Using Periodic ROM

The results for the stability analysis for both the aerodynamic stability, which is obtained by calculating the monodromy matrix for the periodic aerodynamic system, and the coupled model periodic stability are presented in Figure 14. A maximum size of 30 was set for the dimensions of the Periodic ROM at each of the 20 time steps. The limit for system stability is the unit circle, and the eigenvalues that were outside of this circle are presented in Figure 15.

Looking at Figures 14 and 15 it can be seen that the eigenvalues in the coupled model that correspond to the aerodynamics are stable, have low frequencies and are mostly highly damped. However, there are two unstable eigenvalue pairs in the coupled flight mechanics. These are close to the unit circle limit and have a low frequency, possibly related to the blade passing frequency of the rotors. There are also two unstable real values, one of which is very close to the stability region and could be due to the choice of ROM size for the model, and another one near $[3.5, 0]$ which will need to be further analysed in future iterations of the coupled periodic stability model.
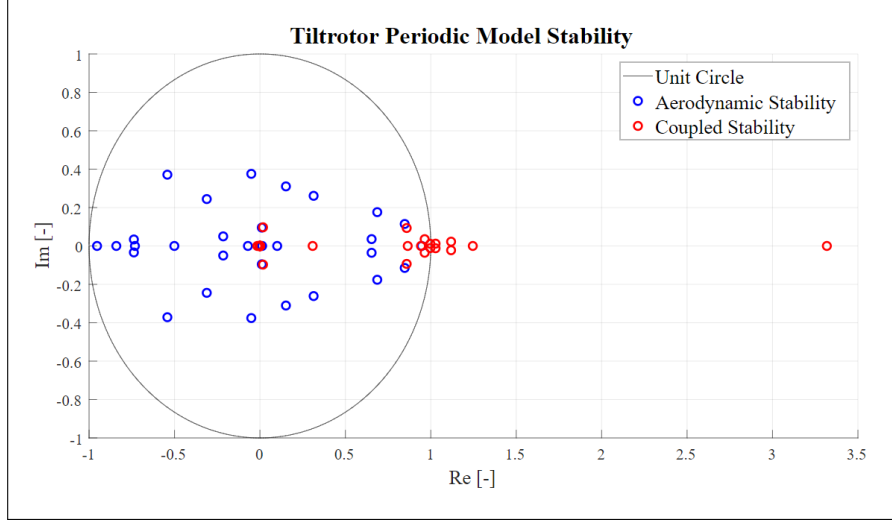
Fig. 14   Tiltrotor periodic system stability.

Classical stability analysis is based on the stability derivatives. The periodic ROM of the tiltrotor aerodynamics was used to obtain the steady-state response of the system. This response was then normalised by the pulse input to obtain the stability derivatives.
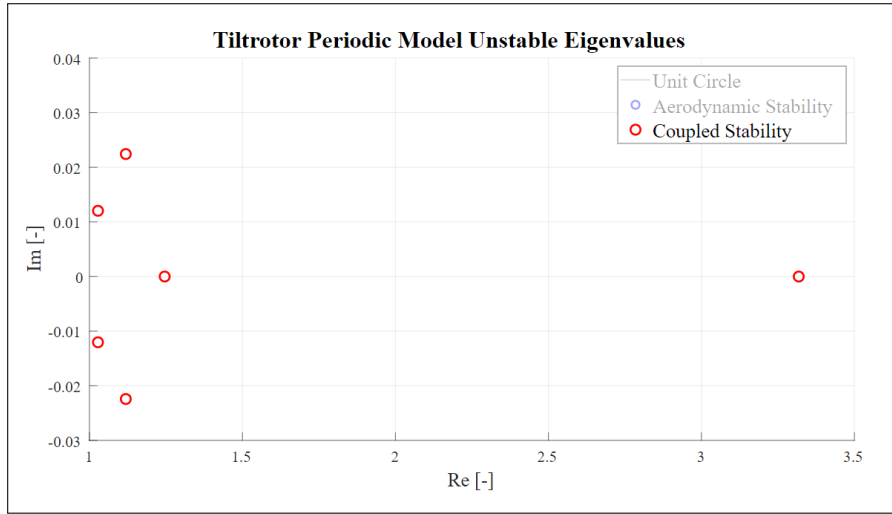
Fig. 15   Eigenvalues outside unit circle. All unstable eigenvalues correspond to the coupled stability model.

Figures 16 and 17 show the stability obtained for the classic flight mechanics model compared to that of the coupled periodic model . Both models present a set of complex eigenvalue pairs near the instability limit, as well as the large real eigenvalue. However, the coupled periodic model is of size 42×42, compared to the 8×8 classical model, therefore it introduces a large number of additional dynamic modes.

Fig. 16   Comparison between classic flight mechanics stability analysis and coupled periodic system stability from the monodromy matrix eigenvalues.
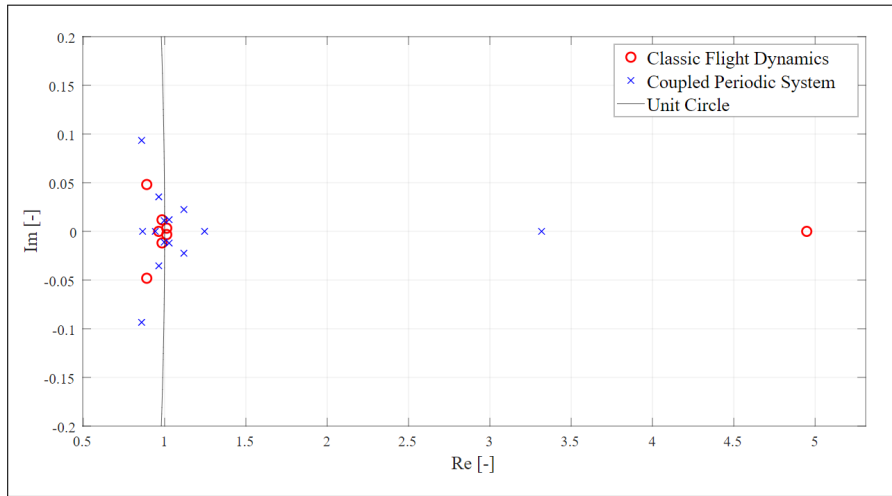
Fig. 17   Zoomed in view of classic flight mechanics eigenvalues.

V. Conclusions

A. Concluding Remarks

Two coupled flight mechanics models have been presented, which are based upon the coupling of a classical flight mechanics system based upon the rigid body equations of motion with a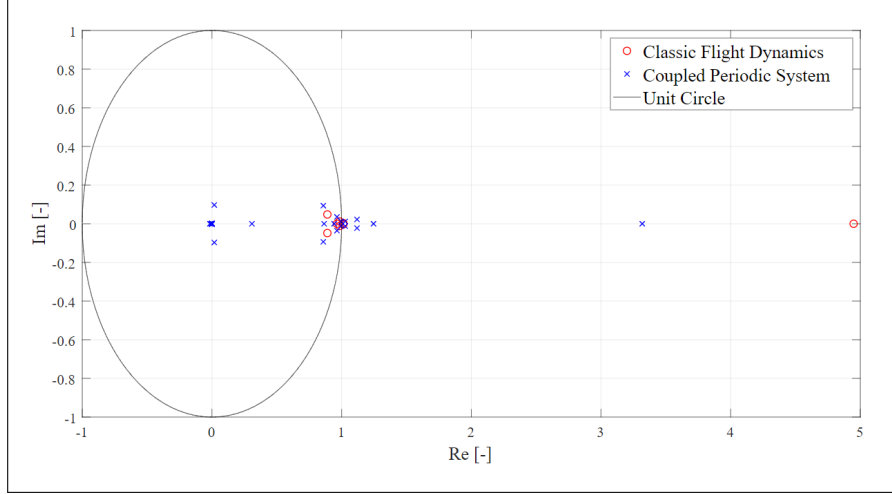 Reduced Order Model (ROM) of an Unsteady Vortex Lattice Method (UVLM). The coupled flight mechanics model allows for not only an analysis of stability which retains the full, linear dynamics of the aerodynamic system in its analysis, but also allows for the reconstruction of flow solutions associated with the predicted unstable motions.

The coupled models have been applied to an analysis of the Bell XV-15 tiltrotor aircraft, a configuration of rotorcraft that have had many stability issues poorly predicted by classical means of analysis. The ROMs were found to give accurate results for vastly reduced computational cost, however it was noted that the ensemble averaged ERA was sensitive to noise in the impulse response data. Moreover, the effects of restarting were found to be detrimental to the accuracy of this ROM.

The inclusion of the the full dynamics of the aerodynamic system was found to have a destabilising effect on the

predicted eigenvalues of the XV-15 when compared to both the equivalent classical analysis utilising the same ROM aerodynamic model and, in the case of the ensemble averaged ROM, the reference models such as the GTRS [14]. The distribution of eigenvalues was seen to be of similar shape to the distributions typical in literature [14, 15, 28], however it was noted that numerical artefacts present in the ROM dynamics may have an influence on these coupled eigenvalues. Finally, an example reconstruction-in-design usage case was presented, and it was shown that the coupled model offers a considerable degree of insight into the aerodynamics of the system and its coupling with the flight mechanics system, proving encouraging for its use in design. Again, the rapid computation offered by the models is highlighted.

B. Recommendations

Four main avenues of research are recommended for future work. The first of which involves the implementation of the reconstruction of the aerodynamic response, using the periodic ROM, of the unstable flight mechanics modes. This will allow a detailed comparison of the two coupled methods presented. Secondly, investigation into the presence of numerical instabilities/artefacts within the ROMs and their effect on the stability of the coupled model should be persued. Methods for treatment of "noise" within the ERA should be investigated further in an effort to improve the robustness of the coupled model. The practical issues with the UVLM, such as implementing a particle deflection scheme, should also be considered for improvement. The mathematical treatment of periodic systems for computationally efficient stability analysis via the ensemble-averaging process should be further investigated as the third avenue of research.

The last avenue to explore involves increasing the fidelity of the XV-15 modelling, primarily via inclusion of blade dynamics and aeroelastics. Modelling of control/drive system dynamics to further improve the capture of aeromechanical coupling [46] would also improve fidelity. There has been a considerable amount of work into the aeroelastic stability (or lack of) within tiltrotors [46, 47], thus the investigation into reconstructing flow solutions associated with aeroelastic phenomena would be an interesting endeavour. Rigid multi-blade flapping dynamics would be a simple first step towards higher fidelity modelling and would be relatively easy to implement, except for some extra effort in the UVLM trimming process. The reader is referred to the multi-blade flapping equations of motion in Johnson [48] for a starting point in this modelling. At these early stages of the coupled model development it is likely that changing the UVLM code for a higher fidelity CFD simulation would only hinder the development. As such it is recommended to make the higher fidelity improvements upon the flight mechanics system due to the much lower computational expense associated with increases in fidelity on this side of the model.

References

[1] Limache, A. C., and Cliff, E. M., "Aerodynamic Sensitivity Theory for Rotary Stability Derivatives," *Journal of Aircraft*, Vol. 37, No. 4, 2000, pp. 676–683. doi:10.2514/2.2651, URL https://doi.org/10.2514/2.2651.

[2] Mader, C. A., and Martins, J. R. R. A., "Computation of Aircraft Stability Derivatives Using an Automatic Differentiation Adjoint Approach," *AIAA Journal*, Vol. 49, No. 12, 2011, pp. 2737–2750. doi:10.2514/1.j051147, URL https://doi.org/10.2514/1.j051147.

[3] Biava, M., Woodgate, M., and Barakos, G. N., "Fully Implicit Discrete-Adjoint Methods for Rotorcraft Applications," *AIAA Journal*, Vol. 54, No. 2, 2016, pp. 735–749. doi:10.2514/1.j054006, URL https://doi.org/10.2514/1.j054006.

[4] Da Ronch, A., Vallespin, D., Ghoreyshi, M., and Badcock, K., "Computation of Dynamic Derivatives Using CFD," *28th AIAA Applied Aerodynamics Conference*, 2010.

[5] Guo, C., and Ren, Y.-X., "On the Calculation of Pitch Damping Stability Derivatives of Aircraft Using Unsteady Sensitivity Equations," *AIAA Atmospheric Flight Mechanics Conference*, American Institute of Aeronautics and Astronautics, 2015. doi:10.2514/6.2015-2559, URL https://doi.org/10.2514/6.2015-2559.

[6] Clean Sky 2 Joint Undertaking, "Clean Sky 2 Joint Technical Programme (V5)," , 2015.

[7] Vertical Flight Society, "Future Vertical Lift," , 2019. URL https://vtol.org/what-we-do/advocacy/future-vertical-lift.

[8] Leonardo, "Leonardo world's No.1 civil helicopter manufacturer secures contracts, eyes new markets and expands training and products," , March 2019. URL https://www.leonardocompany.com/en/press-release-detail/-/detail/leonardo-world-s-no-1-civil-helicopter-manufacturer-08-03-19.

[9] Wernicke, K., and Fischer, J., "An Evaluation of Advanced Rotorcraft Configurations for Emerging Military Applications," *American Helicopter Society 37th Annual Forum*, ????

[10] Parsons, D., "Report: Downwash Likely Culprit In Fatal V-22 Crash Off Australia," , 2018. URL https://www.rotorandwing.com/2018/05/24/report-downwash-likely-culprit-fatal-v-22-crash-off-australia/.

[11] Agenzia Nazionale per la Sicurezza del Volo, *Final Report - Accident occurred to the AgustaWestland AW609 aircraft registration marks N609AG, in Tronzano Vercellese (VC), on the 30th of October, 2015*, 2017.

[12] Tadghighi, H., and Ganesh Rajagopalan, R., "A User's Manual for ROTTILT Solver: Tiltrotor Fountain Flow Field Prediction," 1999. URL https://ntrs.nasa.gov/search.jsp?R=19990026295.

[13] Polak, D. R., Rehm, W., and George, A. R., "Effects of an Image Plane on the Tiltrotor Fountain Flow," *American Helicopter Society 2nd International Aeromechanics Specialists' Meeting*, 1999. URL https://doi.org/10.4050/JAHS.45.90.

[14] Ferguson, S. W., "Development and Validation of a Simulation for a Generic Tilt-Rotor Aircraft," Tech. rep., NASA, 1989. URL https://rotorcraft.arc.nasa.gov/Publications/files/CR-166537_883.pdf.

[15] Kleinhesselink, K. M., "Stability and Control Modeling of Tiltrotor Aircraft," Master's thesis, University of Maryland, 2007.

[16] Maisel, M., and Tilt Rotor Project Office Staff, "NASA/ARMY XV-15 Tilt Rotor Research Aircraft Familiarization Document," Tech. rep., NASA Ames Research Center and US Army Air Mobility R&D Laboratory, 1975. URL https://ntrs.nasa.gov/archive/nasa/casi.ntrs.nasa.gov/19750016648.pdf.

[17] Padfield, G. D., *Helicopter Flight Dynamics*, 2nd ed., 2007.

[18] Etkin, B., and Reid, L. D., *Dynamics of Flight: Stability and Control*, 3rd ed., 1996.

[19] Roth, M., "Vortex Lattice Methods for Aerospace Design," Ph.D. thesis, University of Bristol, December 2016.

[20] Murua, J., Palacios, R., and Graham, J. M. R., "Applications of the unsteady vortex-lattice method in aircraft aeroelasticity and flight dynamics," *Progress in Aerospace Sciences*, Vol. 55, 2012, pp. 46–72.

[21] Matos, C. A. M., "Download Reduction on a Wing-Rotor Configuration," Ph.D. thesis, Georgia Institute of Technology, 2001.

[22] Fejtek, I. G., "Navier-Stokes flowfield computation of wing/rotor interaction for a tilt rotor aircraft in hover," Ph.D. thesis, Stanford University, 1992.

[23] Droandi, G., Zanotti, A., and Gibertini, G., "Aerodynamic Interaction between Rotor and Tilting Wing in Hovering Flight Condition," *Journal of the American Helicopter Society*, Vol. 60, No. 4, 2015, pp. 1–20. doi:10.4050/jahs.60.042011.

[24] Katz, J., and Plotkin, A., *Low-Speed Aerodynamics*, 2nd ed., Cambridge Aerospace Series, Cambridge University Press, 2001, Chap. 13. doi:10.1017/CBO9780511810329.

[25] Gaitonde, A. L., and Jones, D. P., "Study of techniques for obtaining continuous models from 2D discrete reduced-order state-space CFD models," *International Journal for Numerical Methods in Fluids*, Vol. 52, No. 11, 2006, pp. 1247–1275. doi:10.1002/fld.1249, URL https://onlinelibrary.wiley.com/doi/abs/10.1002/fld.1249.

[26] Tang, D., Kholodar, D., Juang, J.-N., and Dowell, E. H., "System Identification and Proper Orthogonal Decomposition Method Applied to Unsteady Aerodynamics," *AIAA Journal*, Vol. 39, No. 8, 2001, pp. 1569–1576. doi:10.2514/2.1482, URL https://doi.org/10.2514/2.1482.

[27] Guckenheimer, J., and Holmes, P., *Nonlinear oscillations, dynamical systems, and bifurcations of vector fields*, Springer, 1983.

[28] Klein, G. D., "Linear Modeling of Tiltrotor Aircraft (In Helicopter and Airplane Modes) for Stability Analysis and Preliminary Design." Tech. rep., NAVAL POSTGRADUATE SCHOOL MONTEREY CA, 1996.

[29] Wales, C., Gaitonde, A., and Jones, D., "Stabilisation of reduced order models via restarting," *International Journal for Numerical Methods in Fluids*, Vol. 73, No. 6, 2013, pp. 578–599. doi:10.1002/fld.3814, URL https://doi.org/10.1002/fld.3814.

[30] Antoulas, A. C., and Sorensen, D. C., "Approximation of large-scale dynamical systems: An overview," Tech. rep., 2001.

[31] Hall, K., Thomas, J. P., and Dowell, E. H., "Proper orthogonal decomposition technique for transonic unsteady aerodynamic flows," *AIAA journal*, Vol. 38, No. 10, 2000, pp. 1853–1862.

[32] Lassila, T., Manzoni, A., Quarteroni, A., and Rozza, G., "Model Order Reduction in Fluid Dynamics: Challenges and Perspectives," 2014, pp. 235–273. URL http://eprints.whiterose.ac.uk/82506/1/LMQR_ROMReview.pdf.

[33] Antoulas, A. C., *Approximation of large-scale dynamical systems*, Vol. 6, Siam, 2005.

[34] Juang, J.-N., and Pappa, R. S., "An eigensystem realization algorithm for modal parameter identification and model reduction," *Journal of guidance, control, and dynamics*, Vol. 8, No. 5, 1985, pp. 620–627. URL https://doi.org/10.2514/3.20031.

[35] Ma, Z., Ahuja, S., and Rowley, C. W., "Reduced-order models for control of fluids using the eigensystem realization algorithm," *Theoretical and Computational Fluid Dynamics*, Vol. 25, No. 1-4, 2011, pp. 233–247. URL https://link.springer.com/article/10.1007/s00162-010-0184-8.

[36] Varga, A., "Balancing Related Methods for Minimal Realization Of Periodic Systems," *Systems and Control Letters*, Vol. 36, 1999, pp. 339–349.

[37] Quaranta, G., Mantegazza, P., and Masarati, P., "Assessing the local stability of periodic motions for large multibody non-linear systems using proper orthogonal decomposition," *Journal of Sound and Vibration*, Vol. 271, No. 3-5, 2004, pp. 1015–1038. doi:10.1016/j.jsv.2003.03.004, URL https://doi.org/10.1016/j.jsv.2003.03.004.

[38] Collaneri, P., and Longhi, S., "The realization problem for linear periodic systems," *Automatica*, Vol. 31, No. 5, 1995, pp. 775–779.

[39] Flamm, D. S., "A new shift-invariant representation for periodic linear systems," *systems & Control Letters*, Vol. 17, 1991, pp. 9–14.

[40] Varga, A., "Computation of Minimal Periodic Realizations of Transfer-Function Matrices," *IEEE Transactions on Automatic Control*, Vol. 49, No. 1, 2004, pp. 146–149. doi:10.1109/tac.2003.821421, URL https://doi.org/10.1109/tac.2003.821421.

[41] Farhood, M., Beck, C. L., and Dullerud, G. E., "Model reduction of periodic systems: a lifting approach," *Automatica*, Vol. 41, No. 6, 2005, pp. 1085–1090. doi:10.1016/j.automatica.2005.01.008, URL https://doi.org/10.1016/j.automatica.2005.01.008.

[42] Varga, A., "Computation of transfer function matrices of periodic systems," *International Journal of Control*, Vol. 76, No. 17, 2003, pp. 1712–1723.

[43] Zhanhua Ma, C. W. R., and Tadmor, G., "Snapshot-based Balanced Truncation for Linear Time-periodic Systems," *IEEE Transactions on Automatic Control*, Vol. 55, No. 02, 2010, pp. 469–473. doi:10.1109/TAC.2009.2036335.

[44] Or, A. C., Speyer, J. L., and Carlson, H. A., "Model reduction of input-output dynamical systems by proper orthogonal decomposition," *Journal of guidance, control, and dynamics*, Vol. 31, No. 2, 2008, pp. 322–328. URL `https://doi.org/10.2514/1.29456`.

[45] Juang, J.-N., and Pappa, R. S., "Effects of noise on modal parameters identified by the eigensystem realization algorithm," *Journal of Guidance, Control, and Dynamics*, Vol. 9, No. 3, 1986, pp. 294–303. URL `https://www.researchgate.net/profile/Richard_Pappa/publication/23885432_Effects_of_noise_on_ERA-identified_modal_parameters`.

[46] Barkai, S., Rand, O., Peyran, R., and Carlson, R., "Modeling and analysis of tilt-rotor aeromechanical phenomena," *Mathematical and Computer Modelling*, Vol. 27, No. 12, 1998, pp. 17 – 43. doi:https://doi.org/10.1016/S0895-7177(98)00071-5, URL `http://www.sciencedirect.com/science/article/pii/S0895717798000715`.

[47] Acree, C., Peyran, R., and Johnson, W., "Rotor Design Options for Improving Tiltrotor Whirl-Flutter Stability Margins," *Journal of the American Helicopter Society*, Vol. 46, No. 2, 2001, pp. 87–95.

[48] Johnson, W., *Rotorcraft Aeromechanics*, Cambridge Aerospace Series, Cambridge University Press, 2013.

A. Linearised Flight Mechanics Equations of Motion

In addition to the nomenclature defined in Section II.A, I terms denote moments of inertia about the body axes (x_b, y_b, z_b) (see Figure 3), and h' terms denote the resultant angular momentum components of any spinning rotors etc. relative to the body axes and expressed about the body axes. Again, barred variables represent the steady-state solutions and un-barred variables represent small perturbations about the steady-state.

$$\dot{x} = u \cdot \cos(\bar{\theta})\cos(\bar{\psi}) + v \cdot \left(\sin(\bar{\phi})\sin(\bar{\theta})\cos(\bar{\psi}) - \cos(\bar{\phi})\sin(\bar{\psi})\right) + w \cdot \left(\cos(\bar{\phi})\sin(\bar{\theta})\cos(\bar{\psi}) + \sin(\bar{\phi})\sin(\bar{\psi})\right)$$
$$+ \phi \cdot \left[\left(\bar{v} + W_y + \bar{W}_y\right)\left(\cos(\bar{\phi})\sin(\bar{\theta})\cos(\bar{\psi}) + \sin(\bar{\phi})\sin(\bar{\psi})\right) + \left(\bar{w} + W_z + \bar{W}_z\right)\left(\cos(\bar{\phi})\sin(\bar{\psi}) - \sin(\bar{\phi})\sin(\bar{\theta})\cos(\bar{\psi})\right) \right]$$
$$+ \theta \cdot \left[\left(\bar{v} + W_y + \bar{W}_y\right)\sin(\bar{\phi})\cos(\bar{\theta})\cos(\bar{\psi}) + \left(\bar{w} + W_z + \bar{W}_z\right)\cos(\bar{\theta})\cos(\bar{\psi}) - \left(\bar{u} + W_x + \bar{W}_x\right)\sin(\bar{\theta})\cos(\bar{\psi}) \right]$$
$$+ \psi \cdot \left[\left(\bar{w} + W_z + \bar{W}_z\right)\left(\sin(\bar{\phi})\cos(\bar{\psi}) - \sin(\bar{\psi})\cos(\bar{\phi})\sin(\bar{\theta})\right) - \left(\bar{v} + W_y + \bar{W}_y\right)\left(\sin(\bar{\psi})\sin(\bar{\phi})\sin(\bar{\theta}) + \cos(\bar{\psi})\cos(\bar{\phi})\right) - \left(\bar{u} + W_x + \bar{W}_x\right)\cos(\bar{\theta})\sin(\bar{\psi}) \right]$$
$$+ W_x \cdot \cos(\bar{\theta})\cos(\bar{\psi}) + W_y \cdot \left(\sin(\bar{\phi})\sin(\bar{\theta})\cos(\bar{\psi}) - \cos(\bar{\phi})\sin(\bar{\psi})\right) + W_z \cdot \left(\cos(\bar{\phi})\sin(\bar{\theta})\cos(\bar{\psi}) + \sin(\bar{\phi})\sin(\bar{\psi})\right)$$

$$\dot{y} = u \cdot \cos(\bar{\theta})\sin(\bar{\psi}) + v \cdot \left(\sin(\bar{\phi})\sin(\bar{\theta})\sin(\bar{\psi}) + \cos(\bar{\phi})\cos(\bar{\psi})\right) + w \cdot \left(\cos(\bar{\phi})\sin(\bar{\theta})\sin(\bar{\psi}) - \sin(\bar{\phi})\cos(\bar{\psi})\right)$$
$$+ \phi \cdot \left[\left(\bar{v} + W_y + \bar{W}_y\right)\left(\cos(\bar{\phi})\sin(\bar{\theta})\sin(\bar{\psi}) - \sin(\bar{\phi})\cos(\bar{\psi})\right) - \left(\bar{w} + W_z + \bar{W}_z\right)\left(\sin(\bar{\phi})\sin(\bar{\theta})\sin(\bar{\psi}) + \cos(\bar{\phi})\cos(\bar{\psi})\right) \right]$$
$$+ \theta \cdot \left[\left(\bar{w} + W_z + \bar{W}_z\right)\cos(\bar{\theta})\cos(\bar{\phi})\sin(\bar{\psi}) + \left(\bar{v} + W_y + \bar{W}_y\right)\cos(\bar{\theta})\sin(\bar{\phi})\sin(\bar{\psi}) - \left(\bar{u} + W_x + \bar{W}_x\right)\sin(\bar{\theta})\sin(\bar{\psi}) \right]$$
$$+ \psi \cdot \left[\left(\bar{w} + W_z + \bar{W}_z\right)\left(\cos(\bar{\psi})\cos(\bar{\phi})\sin(\bar{\theta}) + \sin(\bar{\psi})\sin(\bar{\phi})\right) + \left(\bar{v} + W_y + \bar{W}_y\right)\left(\cos(\bar{\psi})\sin(\bar{\phi})\sin(\bar{\theta}) - \sin(\bar{\psi})\cos(\bar{\phi})\right) + \left(\bar{u} + W_x + \bar{W}_x\right)\cos(\bar{\psi})\cos(\bar{\theta}) \right]$$
$$+ W_x \cdot \cos(\bar{\theta})\sin(\bar{\psi}) + W_y \cdot \left(\sin(\bar{\phi})\sin(\bar{\theta})\sin(\bar{\psi}) + \cos(\bar{\phi})\cos(\bar{\psi})\right) + W_z \cdot \left(\cos(\bar{\phi})\sin(\bar{\theta})\sin(\bar{\psi}) - \sin(\bar{\phi})\cos(\bar{\psi})\right)$$

$$\dot{z} = - u \cdot \sin(\bar{\theta}) + v \cdot \sin(\bar{\phi})\cos(\bar{\theta}) + w \cdot \cos(\bar{\phi})\cos(\bar{\theta}) + \phi \cdot \left[\left(\bar{v} + W_y + \bar{W}_y\right)\cos(\bar{\phi})\cos(\bar{\theta}) - \left(\bar{w} + W_z + \bar{W}_z\right)\sin(\bar{\phi})\cos(\bar{\theta}) \right]$$
$$- \theta \cdot \left[\left(\bar{u} + W_x + \bar{W}_x\right)\cos(\bar{\theta}) + \left(\bar{v} + W_y + \bar{W}_y\right)\sin(\bar{\theta})\sin(\bar{\phi}) + \left(\bar{w} + W_z + \bar{W}_z\right)\sin(\bar{\theta})\cos(\bar{\phi}) \right] - W_x \cdot \sin(\bar{\theta}) + W_y \cdot \sin(\bar{\phi})\cos(\bar{\theta}) + W_z \cdot \cos(\bar{\phi})\cos(\bar{\theta})$$

$$\dot{u} = \frac{X}{m} + v \cdot \bar{r} - w \cdot \bar{q} - \theta \cdot g\cos(\bar{\theta}) - q \cdot \left(\bar{w} + W_z + \bar{W}_z\right) + r \cdot \left(\bar{v} + W_y + \bar{W}_y\right) + W_y \cdot \bar{r} - W_z \cdot \bar{q} - \dot{W}_x$$

$$\dot{v} = \frac{Y}{m} - u \cdot \bar{r} + w \cdot \bar{p} + \phi \cdot g\cos(\bar{\theta})\cos(\bar{\phi}) - \theta \cdot g\sin(\bar{\theta})\sin(\bar{\phi}) + p \cdot \left(\bar{w} + W_z + \bar{W}_z\right) - r \cdot \left(\bar{u} + W_x + \bar{W}_x\right) - W_x \cdot \bar{r} + W_z \cdot \bar{p} - \dot{W}_y$$

$$\dot{w} = \frac{Z}{m} + u \cdot \bar{q} - v \cdot \bar{p} - \phi \cdot g\cos(\bar{\theta})\sin(\bar{\phi}) - \theta \cdot g\sin(\bar{\theta})\cos(\bar{\phi}) - p \cdot \left(\bar{v} + W_y + \bar{W}_y\right) + q \cdot \left(\bar{u} + W_x + \bar{W}_x\right) + W_x \cdot \bar{q} - W_y \cdot \bar{p} - \dot{W}_z$$

$$\dot{\phi} = \phi \cdot \tan(\bar{\theta})\left(\bar{q}\cos(\bar{\phi}) - \bar{r}\sin(\bar{\phi})\right) + \theta \cdot \left(\bar{q}\sin(\bar{\phi}) + \bar{r}\cos(\bar{\phi})\right)\left(1 + \tan^2(\bar{\theta})\right) + p + q \cdot \sin(\bar{\phi})\tan(\bar{\theta}) + r \cdot \cos(\bar{\phi})\tan(\bar{\theta})$$

$$\dot{\theta} = q \cdot \cos(\bar{\phi}) - r \cdot \sin(\bar{\phi}) - \phi \cdot \left(\bar{q}\sin(\bar{\phi}) + \bar{r}\cos(\bar{\phi})\right)$$

$$\dot{\psi} = \phi \cdot \sec(\bar{\theta})\left(\bar{q}\cos(\bar{\phi}) - \bar{r}\sin(\bar{\phi})\right) + \theta \cdot \tan(\bar{\theta})\sec(\bar{\theta})\left(\bar{q}\sin(\bar{\phi}) + \bar{r}\cos(\bar{\phi})\right) + q \cdot \sin(\bar{\phi})\sec(\bar{\theta}) + r \cdot \cos(\bar{\phi})\sec(\bar{\theta})$$

$$\dot{p} = \frac{p\left[\bar{q} \cdot I_{zx}\left(I_x + I_z - I_y\right) - I_{zx} \cdot h'_y\right] + q\left[\bar{r}\left(I_z I_y - I_z^2 - I_{zx}^2\right) + \bar{p} \cdot I_{zx}\left(I_x - I_y + I_z\right) + h'_x I_{zx} - h'_z I_z\right] + r\left[\bar{q}\left(I_y I_z - I_z^2 - I_{zx}^2\right) + h'_y I_z\right] + L \cdot I_z + N \cdot I_{zx}}{I_x \cdot I_z - I_{zx}^2}$$

$$\dot{q} = \frac{p\left[\bar{r}\left(I_z - I_x\right) - 2I_{zx}\bar{p} + h'_z\right] + r\left[\bar{p}\left(I_z - I_x\right) + 2I_{zx}\bar{r} - h'_x\right] + M}{I_y}$$

$$\dot{r} = \frac{p\left[\bar{q}\left(I_x^2 - I_x \cdot I_y + I_{zx}^2\right) - h'_y \cdot I_x\right] + q\left[\bar{p}\left(I_x^2 - I_x \cdot I_y + I_{zx}^2\right) + \bar{r} \cdot I_{zx}\left(I_y - I_x - I_z\right) + h'_x \cdot I_x - h'_z I_{zx}\right] + r\left[\bar{q} \cdot I_{zx}\left(I_y - I_x - I_z\right) + h'_y \cdot I_{zx}\right] + L \cdot I_{zx} + N \cdot I_x}{I_x \cdot I_z - I_{zx}^2}$$

B. Formulation of the Equivalent Classical Model

For a direct comparison between the coupled model and current stability analysis techniques independent of the aerodynamic model fidelity, a classical analysis was performed as per chapter 4.3 of [17]. Classical analysis techniques assume that each of the 6 aerodynamic forces/moments can be represented by a series of partial derivatives (called aerodynamic derivatives) with respect to the input, multiplied by the respective input (i.e. an extension of the linearity assumption). For example, for the stick-fixed response the X force could be written as:

$$X = \frac{\partial X}{\partial x}x + \frac{\partial X}{\partial y}y + \frac{\partial X}{\partial z}z + \frac{\partial X}{\partial u}u + \frac{\partial X}{\partial v}v + \frac{\partial X}{\partial w}w + \frac{\partial X}{\partial \phi}\phi + \frac{\partial X}{\partial \theta}\theta + \frac{\partial X}{\partial \psi}\psi + \frac{\partial X}{\partial p}p + \frac{\partial X}{\partial q}q + \frac{\partial X}{\partial r}r \tag{50}$$

Again, given zero control inputs, this allows for the state-space equation in Equation (3) to simply become $\dot{\underline{x}}_{FM} = A_c \underline{x}_{FM}$ where the A_c matrix contains all of these aerodynamic derivatives, and the kinematics/inertial terms from A_{FM} and E_{FM}. Classically, the assumption is then made that the aerodynamic loads are not functions of the state variables x, y, z and ψ, which allows us to remove these from the system and reduce the problem from 12 to just 8 state variables such that A_c is an 8 by 8 square matrix.

Padfield [17] covers in detail the process of classically obtaining these aerodynamic derivatives, however for our purposes we require a direct comparison between the stability models themselves and thus we extract the derivatives from the ROM aerodynamics. Once converged to steady-state for an input $\underline{x}_{FM}$ we have by definition no rate of change of the aerodynamic state variables, and thus the continuous aerodynamics from Equation (8) become:

$$\dot{\underline{x}}_{A,r} = A_A \underline{x}_{A,r} + B_A \underline{x}_{FM} = \underline{0} \tag{51}$$

$$\underline{x}_{A,r} = -A_A^{-1} B_A \underline{x}_{FM} \tag{52}$$

Thus:

$$\underline{y}_A = -C_A A_A^{-1} B_A \underline{x}_{FM} \tag{53}$$

As the aerodynamic model outputs forces and inputs flight mechanics states at a different frame of reference to the flight mechanics system, this needs transforming back onto the body axes for classical stability analysis. Thus, about the body axes:

$$\underline{y}_A = -R^{-1} C_{A,r} A_{A,r}^{-1} B_{A,r} L \underline{x}_{FM} \tag{54}$$

From Equations (50) and (54) it can be seen that according to the prior assumptions regarding expansion of the aerodynamic derivatives, the matrix $\left[-R^{-1} C_{A,r} A_{A,r}^{-1} B_{A,r} L \right]$ represents the aerodynamic derivatives calculated via the ROM aerodynamics. The A_c classical system matrix given by Equation 4.44 in [17] is then formed by non-dimensionalising and then substituting the necessary derivatives. This A_c represents a typical classical analysis with similar rigid flight mechanics to that used in this work, noting however the additional assumptions made by Padfield such as certain aerodynamic derivatives being negligible and thus approximated to zero. Thus, an equivalent classical model to the coupled model is formed, which is independent of the aerodynamic model fidelity and can be used for direct comparison of the methods. It can be seen that the classical analysis in theory should lose a significant amount of the fidelity offered by the aerodynamic system in Equation (8) by approximating it as a first-order Taylor expansion, whereas the coupled model retains this behaviour.

C. Balanced realisation of the gramian product

For a balanced realisation, need $S_k T_k = I$. The matrices T_k and S_k have been previously defined as:

$$S_k = \Sigma_k^{-1/2} U_k^T \tilde{F}_k$$
$$T_k = \tilde{G}_k V_k \Sigma_k^{-1/2} \tag{55}$$

Performing a Singular Value Decomposition of the cross gramian we obtain $\tilde{F}_k \tilde{G}_k = U_k \Sigma_k V_k^T$. Therefore, by expanding the condition for a balanced realisation and substituting the cross gramian with the SVD:

$$\begin{aligned}
S_k T_k &= \Sigma_k^{-1/2} U_k^T \tilde{F}_k \tilde{G}_k V_k \Sigma_k^{-1/2} \\
&= \Sigma_k^{-1/2} U_k^T U_k \Sigma_k V_k^T V_k \Sigma_k^{-1/2} \\
&= I
\end{aligned} \tag{56}$$

It is possible to show that this transformation matrix will give the Hankel singular values when applied to the controllability and observability gramians. First for the controllability gramian:

$$\begin{aligned}
S_k \tilde{G}_k \tilde{G}_k^T S_k^T &= \Sigma_k^{-1/2} U_k^T \tilde{F}_k \tilde{G}_k \tilde{G}_k^T \tilde{F}_k^T U_k \Sigma_k^{-1/2} \\
&= \Sigma^{-1/2} U_k^T \left(U_k \Sigma_k V_k^T \right) \left(V_k \Sigma_k U_k^T \right) U_k \Sigma^{-1/2} \\
&= \Sigma_k
\end{aligned} \tag{57}$$

And for the observability gramian:

$$\begin{aligned}
T_k^T \tilde{F}_k^T \tilde{F}_k T_k &= \Sigma_k^{-1/2} V_k^T \tilde{G}_k^T \tilde{F}_k^T \tilde{F}_k \tilde{G}_k V_k \Sigma_k^{-1/2} \\
&= \Sigma^{-1/2} V_k^T \left(V_k \Sigma_k U_k^T \right) \left(U_k \Sigma_k V_k^T \right) V_k \Sigma^{-1/2} \\
&= \Sigma_k
\end{aligned} \tag{58}$$